Chapter 5

HYBRID CODES

Methods and Applications

D. Winske and N. Omidi

Summary

In this chapter we discuss "hybrid" algorithms used in the study of low frequency electromagnetic phenomena, where one or more ion species are treated kinetically via standard PIC methods used in particle codes and the electrons are treated as a single charge neutralizing massless fluid. Other types of hybrid models are possible, as discussed in Winske [1985] and Quest [1989], but hybrid codes with particle ions and massless fluid electrons have become the most common for simulating space plasma physics phenomena in the last decade, as we shall show later.

This chapter is divided into four sections. The first three subsections are devoted to the basics of hybrid codes and simple applications and is aimed at the uninitiated user. We begin in Section 5.1 with some examples of where hybrid codes have been found to be most useful and lay out the basic underlying assumptions and equations of the model. Then we discuss in Section 4.2 the details of a simple one-dimensional hybrid algorithm. The code itself (as well as a simple operator's guide) is included on the diskette enclosed with this book or is available via e-mail from the authors. In Section 4.3 we go on to describe the physics and numerics of some simple applications of electromagnetic ion beam instabilities in a periodic system as well as to briefly discuss the extension of the code to nonperiodic problems. These examples serve as the test problems for the version of the code included on the diskette. The last part of the chapter (Section 4.4) is devoted to more advanced topics; the discussion is brief and aimed at readers with some prior experience with hybrid codes. The topics to be discussed include alternative methods to solve the electromagnetic field equations in the massless electron fluid approximation and extensions of the

algorithm to two and three spatial dimensions. Some recent state of the art
two and three dimensional hybrid simulations of space plasma phenomena are
also briefly described. This part concludes with some short comments on future
trends in the development and uses of hybrid codes.

5.1 Basics

5.1.1 Introduction

When one looks at spacecraft data, *e.g.*, time series of magnetic field compo-
nents, plasma velocity moments, wave intensities at various frequencies, *etc.*,
from anywhere in the heliosphere or the magnetosphere, one is usually over-
whelmed by their complexity. It is evident that a wide variety of physical
phenomena are taking place on a vast range of time and distance scales. It falls
on the shoulders of the space scientist to separate out the various effects and
their relevant temporal and/or spatial scales. In part this is done by filtering
the data, either by "eye-balling" it or using more sophisticated techniques in
order to emphasize certain characteristics. One also develops theoretical models
to explain the presence of these prominent features. The role of simulations is
to help develop or verify the models by including limited physics and/or solving
a reduced set of equations to test the underlying assumptions. Simulations are
also important for extending the models, by including in a self consistent man-
ner time dependence, nonlinear and nonlocal effects, and other aspects of the
problem not readily amenable to analytic theory. Also, simulations by them-
selves can identify key elements that are needed to construct an appropriate
theoretical explanation. Rather than continuing to deal in abstractions, we
turn to some specific examples from space physics.

   One well studied example of this kind of complexity is the region upstream
of the Earth's bow shock, known as the foreshock. A special issue of *Journal of
Geophysical Research* (Vol. 86, June, 1981) devoted primarily to observations
in this region illustrates the broad range of complex phenomena. [The reader
may wish to glance at some of the figures in representative articles by Hoppe *et
al.* (1981), Paschmann *et al.* (1981), Anderson *et al.* (1981), *etc.* in this issue.]

   The foreshock is characterized by particles that are leaked or reflected from
the shock which stream back into the solar wind. The geometry of the shock
causes one part of the foreshock to be dominated by backstreaming electrons
("electron foreshock"), while another, larger part of the foreshock is dominated
by backstreaming ions ("ion foreshock"). As one might expect, the phenomena
observed in the two foreshocks are quite distinct. Of interest to us here is the
ion foreshock, which the wave data clearly show, is dominated in some region by
well defined low frequency (ULF) waves with characteristic period of one-half to
one minute. In some parts of the ion foreshock the waves are fairly regular and
rather low amplitude (fluctuating magnetic field $\delta B \ll B=$ mean value), while

in other parts of the foreshock the waves are larger ($\delta B \sim B$) and less regular in appearance [Hoppe *et al.*, 1981]. The corresponding characteristics of the backstreaming ions are also different: beam-like where the waves are small and regular, and more scattered ("diffuse") where the waves are large and irregular [Paschmann *et al.*, 1981]. Although the rest frame frequencies of the waves are much smaller than the ion gyroperiod ($\omega \ll \Omega_i$) and the wavelengths (typically $\sim 1 R_E$) are much larger than the ion thermal gyroradius ($\rho_i \sim 100$km), fluid theory cannot be applied to these waves, because kinetic effects due to the backstreaming ions modify the dispersive properties of the waves.

As we discuss in somewhat greater detail later, theory has shown that these waves can be generated by an electromagnetic ion beam instability, involving the relative field aligned drift of the backstreaming ions with the solar wind [Barnes, 1970; Gary *et al.*, 1981]. The wave generation process involves a cyclotron resonance of the beam ions with an electromagnetic wave. This mechanism has been shown to be most consistent with the observations. In the instability the electrons play no significant role, and observations show no interesting electron effects (*e.g.*, acceleration, heating, or high frequency waves) in the ion foreshock. It thus suggests that the relevant phenomena can be studied numerically using a model in which the electrons are treated passively, as a charge neutralizing massless electron fluid, but ion kinetic effects are necessary, *i.e.*, a hybrid description. As we show later, indeed the hybrid simulations [Winske and Leroy, 1984a] reproduce the essential features of the (linear) theory and demonstrate that nonlinear processes are needed to explain many of the foreshock observations.

A second example of spacecraft observations that indicate the usefulness of a hybrid model algorithm is the Earth's bow shock, or collisionless shocks in general. Again, the observations display great complexity on many time and spatial scales [see the recent AGU monographs on collisionless shocks (Stone and Tsurutani, 1985; Tsurutani and Stone, 1985)]. Closer examination of the data indicates that ion scales determine the overall shock structure [*e.g.*, Scudder *et al.*, 1986], suggesting that ion dissipation plays a dominant role at the shock, while electrons are of secondary importance. Hybrid simulations demonstrate and observations verify that the dissipation arises from the reflection of a fraction of the incident ions, which then couple to the downstream ions by means of electromagnetic instabilities. The reflection process has been dramatically illustrated in one dimensional hybrid simulations of a perpendicular shock [Leroy *et al.*, 1981]. More recently the simulations have been instrumental in understanding the complex nature of the quasi-parallel shock [Burgess, 1989]. We will briefly return to the application of hybrid codes to shocks later in this chapter [also see Winske and Leroy (1984b) and Winske (1985)].

A third example involves the heating of minority ions to suprathermal energies in the equatorial magnetosphere by ion cyclotron waves. Linear theory suggests that the waves are generated by an instability involving a weak temper-

ature anisotropy $(T_\perp/T_\parallel > 1)$ in a small population of hot protons, consistent with the observations at geosynchronous orbit [*e.g.*, Mauk *et al.*, 1981; Gendrin *et al.*, 1984]. To study the nonlinear evolution of the waves and the heating mechanism, simulations are necessary. Linear theory shows that the electrons play no significant role in the properties of the waves, again suggesting a hybrid description to be most appropriate. Hybrid simulations have been carried out [Omura *et al.*, 1985] that nicely display the growth of the instability and the development of the ion cyclotron waves. More importantly, the calculations show that the heating of the minority ions is a two step process. Initially, the ions heat primarily in the perpendicular direction until the parallel velocity becomes on the order of the resonance velocity, at which time strong heating occurs. This type of electromagnetic ion cyclotron beam anisotropy instability has also been studied in the solar wind [Gary *et al.*, 1976] and in the magnetosheath [Tanaka, 1985]. Also see Gary and Schriver [1987] for other examples and theoretical background.

Thus, these three examples (many others could also be cited) show that there is good observational evidence for considering a hybrid model with kinetic ions and massless fluid electrons for studying magnetospheric plasmas.

5.1.2 Equations

In modeling plasma phenomena one needs to decide how to describe the electric and magnetic fields as well as the plasma species (electrons and ions). In the hybrid model these are: (1) electromagnetic fields in the Darwin limit, (2) massless fluid electrons, and (3) kinetic ions. Specifically, the following assumptions and equations are used.

(1) Maxwell's equations in the low frequency approximation, which implies the displacement current is neglected in Ampere's law

$$\vec{\nabla} \times \vec{B} = \frac{4\pi}{c}\vec{J} \tag{5.1}$$

supplemented by Faraday's law

$$\vec{\nabla} \times \vec{E} = -\frac{1}{c}\frac{\partial \vec{B}}{\partial t} \tag{5.2}$$

and

$$\vec{\nabla} \cdot \vec{B} = 0 \tag{5.3}$$

(2) Fluid equations for the electrons including finite electron temperature (T_e) in the limit of zero electron mass. The electron momentum equation is thus

$$\frac{\partial}{\partial t}n_e m_e \vec{V}_e = 0 = -en_e(\vec{E} + \frac{\vec{V}_e \times \vec{B}}{c}) - \vec{\nabla} \cdot \mathbf{P_e} + en_e\mathbf{R} \cdot \vec{J} \tag{5.4}$$

with electron pressure tensor

$$\mathbf{P_e} = n_e T_e \mathbf{1} \tag{5.5}$$

(Tensors are denoted by bold face.) We have assumed isotropic pressure for simplicity here, but this is not required. The last term in (5.4) represents the effect of the collisional drag between the electrons and ions, where $\mathbf{R}$ is the resistivity (tensor) that describes short wavelength, high frequency anomalous wave-particle scattering due to $m_e \neq 0$, $\omega \gg \Omega_i$ instabilities not explicitly included in the hybrid model. Hereafter, for simplicity we will take the resistivity to be a scalar, *i.e.*, $\mathbf{R} = \eta \mathbf{1}$.

An equation of state is needed to supplement (5.5), as discussed later. Quasi-neutrality is also assumed, which implies

$$n_e = n_i \tag{5.6}$$

as we discuss later. Equation (5.6) replaces Poisson's equation that would usually be included with Eqs. (5.1-5.3). As we show later, the longitudinal part of the electric field that is usually obtained from Poisson's equation is calculated using one component of (5.4) along with (5.6).

(3) Kinetic treatment of the ions so that for individual particles (subscript p)

$$\frac{dx_p}{dt} = v_{xp} \tag{5.7}$$

$$m_p \frac{d\vec{v}_p}{dt} = e(\vec{E} + \frac{\vec{v}_p \times \vec{B}}{c}) - e\eta\vec{J} \tag{5.8}$$

The last term in (5.8) balances the corresponding term in the electron momentum equation (5.4).

Given the equations of the model, their numerical implementation is the next task to be discussed.

5.2 Simple One-Dimensional Hybrid Code

We next discuss the contents of a simple one-dimensional hybrid code. Details of the various parts of the algorithm are found in several places [Morse and Nielson, 1971; Sgro and Nielson, 1976; Winske and Leroy, 1984b; Winske, 1985; Forslund, 1985]. Some of the discussions are repeated here in order to have a reasonably complete, self contained presentation. As with full particle codes, there are a number of different ways to treat the particles, difference the field equations, *etc.* Thus, the method we present is but one workable solution that offers the reader a perhaps different perspective to the problem of simulating kinetic plasma phenomena.

The basic ingredients of the hybrid code are: (A) units and spatial grid, (B) ion dynamics, (C) treatment of the electrons, (D) solution of the electromagnetic

fields, (E) initialization, and (F) diagnostics. We discuss each of these points in turn.

5.2.1   Units and spatial grid

As discussed in Section 5.1, hybrid codes are most useful in treating electromagnetic phenomena on ion time and spatial scales, *i.e.*, characteristic times $\geq \Omega_i^{-1}$ and distances $\geq c/\omega_i$ or ρ_i. We thus consider a system of length $XMAX$ c/ω_i, with single dimension coordinate x, *i.e.*, $0 \leq x \leq XMAX$. Although there is only one spatial coordinate, all velocity and field components are retained in the calculation. In this system we have one or more ion species, each characterized by an initial density $n_j(x)$, mass m_j, charge e_j and velocity distribution $F_j(\vec{v})$. As we are interested in magnetized phenomena, there is also a background magnetic field $\vec{B}_o(x)$. From these quantities we can define (in various ways depending on the problem) an ion gyrofrequency (Ω_i) and an ion plasma frequency (ω_i). Then using the speed of light (c) as the unit of velocity, we can define a spatial scale in terms of c/ω_i, and a time scale in terms of ω_i^{-1}. In part this choice of normalization is historical (based on the normalization used in electromagnetic particle codes). One could instead normalize the velocity to the Alfven (v_A) speed and the time to the inverse ion gyrofrequency. In the simple class of problems we discuss later, the plasma consists of two ion species that are homogeneous in space with density n_1 and n_2 (with $n_o = n_1 + n_2$), charge e_o(=charge of the proton), and masses $m_1/m_o = m_2/m_o = 1$ (m_o =mass of the proton). In this case we then define

$$\omega_i^2 \;=\; 4\pi e_o^2 n_o/m_o \tag{5.9}$$

and

$$\Omega_i \;=\; e_o B_o/m_o c \tag{5.10}$$

In these units the electromagnetic fields are expressed as $e_o\vec{E}/m_o c\omega_i$, $e_o\vec{B}/m_o c\omega_i$; with this choice there are no constants ($4\pi, c$, *etc.*) in Maxwell's equations. In the low frequency (Darwin) approximation, $\omega_i/\Omega_i = c/v_A$ is arbitrary; in a practical sense it can be determined by choosing the system density and magnetic field in real units (cm^{-3}, nT, *etc.*). The direction of the background magnetic field is also arbitrary, *i.e.*, it does not have to be aligned along x. Usually we take $\vec{B}$ in the $x - z$ plane, making an angle θ with respect to the x axis.

The spatial domain is subdivided into NX computational cells of equal length, $\Delta x \equiv HX = XMAX/NX$. The system length is based on physical considerations, *e.g.*, longer than the anticipated wavelengths of instabilities, widths of boundary layers, *etc.* The cell size is then chosen to resolve these characteristic phenomena, *i.e.*, enough cells to well describe the wavelengths of unstable modes, discontinuities, *etc.* The typical rule of thumb is that $HX >$
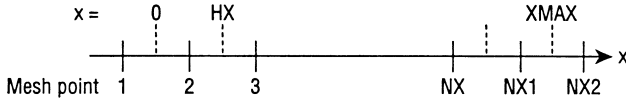
Figure 5.1: Spatial grid for the 1-D code.

$0.1c/\omega_i$ and HX can be as large as several c/ω_i for long wavelength phenomena. The lower limit results from the assumption of massless electrons and hence the elimination of c/ω_e scales ($\omega_e^2 = 4\pi n_o e_o^2/m_e$). As a practical guide, $XMAX$ and HX are chosen together so that NX is a reasonable number (typically $10^2 - 10^3$) that yields a modest total number of simulation particles (usually one uses 20-100 particles/cell), as will become evident when the applications are discussed.

The spatial grid is made up of $NX + 2 = NX2$ mesh points (Figure 5.1). Mesh points $2, 3, ...NX + 1(= NX1)$ define the centers of the NX cells in the physical domain. In addition, there is a "ghost cell" at each end of the system, described by mesh point 1 and $NX2$ respectively. As will be shown shortly, the ghost cells are important for assigning the particles' contributions to the density and current and in imposing boundary conditions on the fields. All source terms (densities and currents) and electromagnetic field components are specified at the mesh points, *i.e.*, the cell centers.

In a similar manner the particles and fields are stepped forward in time with a constant time step DT= $\omega_i \Delta t$. In typical leap-frog fashion, the particle positions and the fields are known at the beginning of each time step, with the velocities of the particles specified at the half time step. Again, the time step should be small enough to resolve phenomena of interest. Because most problems involve low frequency effects (characteristic frequency $\omega \ll \Omega_i$), the time step is limited by the condition that ion gyromotion is well resolved ($\Omega_i \Delta t \leq 0.2$) as well as keeping particle increments to some fraction of one computational cell per time step (typically, $V_{max}\Delta t \leq \Delta x/2$). Here V_{max} represents the maximum speed of the ions (*e.g.*, drift or thermal speed), or if ion energetization occurs, by the speed of the energetic ions.

5.2.2   Ion dynamics

The ions are treated by standard particle-in-cell methods [Forslund, 1985]. Particles have a square shape, an extent HX, and simple linear interpolation is used to compute the forces acting on the particles as well as how the density and currents are accumulated on the grid. To advance an ion in time [Eqs. (5.7-5.8)] from time step N to time step $N + 1$, we first advance the velocity from

its known value $\vec{v}_p^{N-1/2}$ to $\vec{v}_p^{N+1/2}$ (superscript denotes time level) via:

$$\vec{v}_p^{N+1/2} = \vec{v}_p^{N-1/2} + \frac{e_s \Delta t}{m_s}(\vec{E}^N + \vec{v}_p^N \times \vec{B}^N) - \frac{e_s \Delta t}{m_s}\eta \vec{J}^N \qquad (5.11)$$

Recall that the last term represents the resistive drag on the ions by the electrons. One can think of it as modifying the electric field felt by an ion and combine it with $\vec{E}$ into an effective electric field $\vec{E}'$. Also, to simplify some of the expressions and for easier comparison with the code, we have expressed quantities in dimensionless code units: velocities in terms of c, time in terms of ω_i^{-1}, density in terms of n_o, the ion charge and mass in terms of the proton charge e_o and mass m_o, and the electric and magnetic fields normalized by $m_o c \omega_i / e_o$. Thus, e_s and m_s are the ion charge and mass normalized to e_o and m_o.

Note that in order for Eq. (5.11) to be time centered, $\vec{v}_p^N$ is used to determine the acceleration by the magnetic field. Since v_p^N is not known explicitly, we use $\vec{v}_p^N = 1/2(\vec{v}_p^{N-1/2} + \vec{v}_p^{N+1/2})$. Then Eq. (5.11) can be solved for $\vec{v}_p^{N+1/2}$, by taking its dot and cross product with $\vec{B}^N$ and substituting back into (5.11) [Forslund, 1985], as shown in Appendix A. This gives

$$\begin{aligned}
\vec{v}_p^{N+1/2} = {} & \frac{1}{1 + h^2 \vec{B} \cdot \vec{B}/4}[\vec{v}_p^{N-1/2}(1 - \frac{h^2}{4}\vec{B} \cdot \vec{B}) \\
& + h(\vec{E}' + \vec{v}_p^{N-1/2} \times \vec{B}) + \frac{h^2}{2}(\vec{E}' \times \vec{B}) \\
& + \frac{h^2}{2}(\vec{B}(\vec{v}_p^{N-1/2} \cdot \vec{B}) + \frac{h^3}{4}(\vec{B}(\vec{E}' \cdot \vec{B}))]
\end{aligned} \qquad (5.12)$$

To order $(\Delta t)^2$, Eq. (5.12) is

$$\begin{aligned}
\vec{v}_p^{N+1/2} = {} & \vec{v}_p^{N-1/2}(1 - \frac{h^2}{2}\vec{B} \cdot \vec{B}) + h(\vec{E}' + \vec{v}_p^{N-1/2} \times \vec{B}) \\
& + \frac{h^2}{2}(\vec{E}' \times \vec{B}) + \frac{h^2}{2}\vec{B}(\vec{v}_p^{N-1/2} \cdot \vec{B})
\end{aligned} \qquad (5.13)$$

where $h = e_s \Delta t / m_s$, $\vec{E}' = \vec{E} - e_s \eta \vec{J}$. Then the particle can be advanced from its position at time step N (x_p^N) to x_p^{N+1}:

$$x_p^{N+1} = x_p^N + v_{p,x}^{N+1/2}\Delta t \qquad (5.14)$$

In Eq. (5.12), $\vec{E}$, $\vec{B}$ are explicitly $\vec{E}^N(x_p^N)$, $\vec{B}^N(x_p^N)$ and are obtained by linear interpolation. For example, if a particle is located at x_p^N, $\vec{E}^N(x_p^N)$ is a linear combination of contributions from cell I and cell $I + 1$ (Figure 5.2)

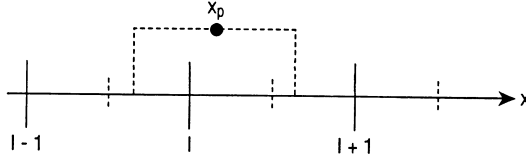$$\vec{E}^N(x_p^N) = \vec{E}_I^N W_I + \vec{E}_{I+1}^N W_{I+1} \qquad (5.15)$$

Figure 5.2: Particle shape and relation to the grid.

where
$$I = INT(x_p/\Delta x + 1.5) \tag{5.16}$$
and $INT(x)$ is the FORTRAN integer truncation function, so that
$$W_{I+1} = x_p/\Delta x + 1.5 - I \tag{5.17}$$
and
$$W_I = 1.0 - W_{I+1} \tag{5.18}$$
(as a simple check, $x_p = 0$ corresponds to a particle lying halfway between mesh point 1 and 2, so that $I = 1$ with $W_1 = W_2 = 0.5$.)

In similar fashion after the particle is moved, its density is accumulated on the grid by the same linear interpolation, again using Eqs. (5.15-5.18) to determine the cells I, $I + 1$ to which it is assigned, with corresponding weights W_I, W_{I+1}. In the scheme used in this version of the hybrid code [Sgro and Nielson, 1976] the currents are also accumulated at the whole time step. To do this, Eq. (5.11) is used with $\vec{E}^N$, $\vec{B}^N$ evaluated at x_p^{N+1} to push the velocities ahead one half time step to collect $\vec{J}^{N+1}$.

Because the particle charge density and current are shared with two cells, it is possible that one of the two cells may be a ghost cell. For example, if $x_p < HX/2$, the source term contribution will be shared between $I = 1$ and $I = 2$ [Eqs. (5.15-5.18)]. After all the particles are moved, we then take the density and currents accumulated in the ghost cells and place them back in the physical cells of the system. How this is done depends on the boundary conditions. In the version of the code being discussed here, periodic boundary conditions are used so that the density and current accumulated in cell $I = 1$ are put in the last physical cell, $I = NX1$, while the density and current in the ghost cell $I = NX2$ are deposited in the first physical cell $I = 2$. For some applications it is useful to smooth the total ion density and current before solving for the electromagnetic fields in order to further reduce the noise levels, as discussed later.

5.2.3 Electrons

The electrons are treated in a most elementary fashion, using the quasi-neutral approximation and a simple equation of state. The quasi-neutral approximation

means that on spatial scales much greater than the electron Debye length, the electron and ion densities are equal, *i.e.*,

$$n_{e,I} = n_{i,I} \tag{5.19}$$

Thus, where the electron density is needed in the field (momentum) equation, one uses n_i, which is found, of course, from moving the ions. The longitudinal electric field, E_x, rather than representing a charge separation electric field, is the field needed to maintain charge neutrality on ion spatial scales.

The continuity equation then implies

$$\vec{\nabla} \cdot \vec{J} = 0 \tag{5.20}$$

or in 1-D

$$J_x = J_{ex} + J_{ix} = \text{const} \tag{5.21}$$

with the constant almost always taken to be zero, implying for $e_s = 1$ used hereafter,

$$V_{ex} = V_{ix} \tag{5.22}$$

In higher dimensions (5.20) is more complex and must be treated more carefully [Hewett, 1980].

The electron equation of state can be treated in a number of ways. For most problems, we have found the electron model has a very small effect on the overall solution. We typically use either

$$T_e(x) = \text{const} \tag{5.23}$$

or

$$T_e(x) = T_{eo}(n_e(x)/n_o)^{\gamma_e-1} \tag{5.24}$$

with $\gamma_e = 5/3$. It is also possible to resistively heat the electrons by solving a heat equation, as discussed by Winske and Leroy [1984b].

Finally, a few comments should be made about the resistivity. η represents wave-particle effects due to high frequency ($\omega > \Omega_i$) plasma instabilities that involve the electron mass, which are not explicitly modeled in the hybrid formulation. One can express the effects of these processes in terms of an "anomalous" electron-ion collision frequency ν_{an}, which is related to the resistivity in the standard way, *i.e.*,

$$\eta = 4\pi\nu_{an}/\omega_e^2 \tag{5.25}$$

In the code η is expressed in dimensionless form

$$\eta_s = \frac{\eta\omega_i}{4\pi} = \frac{\nu_{an}}{\Omega_e}\frac{\Omega_i}{\omega_i} \tag{5.26}$$

A practical way to estimate the size of η_s is to express it in terms of a resistive length

$$L_\eta \; = \; \frac{\eta c^2}{4\pi V} \; = \; \frac{\eta_s}{V/v_A}\frac{\omega_i}{\Omega_i}\frac{c}{\omega_i} \tag{5.27}$$

where V is some characteristic flow velocity of the problem. One typically chooses L_η to be some fraction of a cell size (e.g., $\leq 0.1\Delta x$). For many problems, as in the examples discussed later, η can be taken to be zero. For other problems (e.g., some shock problems), a finite η is very useful in eliminating unwanted high frequency noise. In such cases typical values for η_s correspond to values of the collision frequency on the order of the lower hybrid frequency, consistent with various types of cross-field instabilities [Leroy et al., 1982; Spicer et al., 1990].

5.2.4 Electromagnetic fields

Given the current and charge density at time step $N + 1$, the transverse (i.e., y and z components) electromagnetic fields $\vec{E}^{N+1}$, $\vec{B}^{N+1}$ are obtained by expressing the fields in terms of the vector potential $\vec{A}^{N+1}$ (see Winske and Leroy [1984b] and Winske [1985]). The x-component (i.e., the longitudinal part) of $\vec{E}^{N+1}$ is easily obtained from (5.4) and in one dimension Eq. (5.3) implies

$$B_x \; = \; \text{const} \tag{5.28}$$

In the following, we discuss the mechanics of solving for $\vec{A}^{N+1}$ in some detail.

Although in general it is possible to express the magnetic field in terms of the vector potential, in a 1-D periodic system it is best to remove the constant part of B_y $(= B_{yc})$ and B_z $(= B_{zc})$ and express only the fluctuating part of $\vec{B}$ in terms of the vector potential $\vec{A}$. We then have for the fluctuating part

$$B_y \; = \; -\partial A_z/\partial x \tag{5.29}$$

$$B_z \; = \; \partial A_y/\partial x \tag{5.30}$$

or in difference form (subscript I represent the mesh point)

$$B_{y,I}^{N+1} \; = \; -(A_{z,I+1}^{N+1} - A_{z,I-1}^{N+1})/2\Delta x \tag{5.31}$$

$$B_{z,I}^{N+1} \; = \; (A_{y,I+1}^{N+1} - A_{y,I-1}^{N+1})/2\Delta x \tag{5.32}$$

The y and z components of the electric field are given by

$$E_y \; = \; -\frac{\partial A_y}{\partial t} \tag{5.33}$$

$$E_z \; = \; -\frac{\partial A_z}{\partial t} \tag{5.34}$$

or

$$E_y^{N+1} = -(A_{y,I}^{N+1} - A_{y,I}^N)/\Delta t \qquad (5.35)$$

$$E_z^{N+1} = -(A_{z,I}^{N+1} - A_{z,I}^N)/\Delta t \qquad (5.36)$$

Ampere's law [Eq. (5.1)] then becomes

$$\frac{\partial^2 A_y}{\partial x^2} = -J_y \qquad (5.37)$$

$$\frac{\partial^2 A_z}{\partial x^2} = -J_z \qquad (5.38)$$

The right hand side of (5.37-5.38) contains the currents, which consist of ion and electron contributions. The ion contributions are obtained directly, along with the density, from moving the ions and collecting the moments. The electron currents are obtained from the y and z components of the electron momentum equation (5.4), assuming a constant η. Then Eqs. (5.37-5.38) become [Winske, 1985]

$$-\frac{\partial^2 A_y}{\partial x^2} = \frac{F_y + \delta F_z}{1 + \delta^2} \qquad (5.39)$$

$$-\frac{\partial^2 A_z}{\partial x^2} = \frac{F_z - \delta F_y}{1 + \delta^2} \qquad (5.40)$$

where

$$F_y = n_i[V_{iy} - \frac{E_z}{B_x} - \frac{V_{ix}(B_y + B_{yc})}{B_x}] \qquad (5.41)$$

$$F_z = n_i[V_{iz} + \frac{E_y}{B_x} - \frac{V_{ix}(B_z + B_{zc})}{B_x}] \qquad (5.42)$$

$$\delta = \frac{n_i \eta_s}{B_x} \qquad (5.43)$$

where all the quantities in (5.39-5.43) are at time level $N + 1$. Then using the expressions for $\vec{E}$ and $\vec{B}$ in terms of $\vec{A}$, Eqs. (5.39-5.40) become the coupled set of equations

$$\frac{\partial^2 A_y}{\partial x^2} = f_1(\frac{\partial A_y}{\partial x}, \frac{\partial A_z}{\partial x}, \frac{\partial A_y}{\partial t}, \frac{\partial A_z}{\partial t}) \qquad (5.44)$$

$$\frac{\partial^2 A_z}{\partial x^2} = f_2(\frac{\partial A_y}{\partial x}, \frac{\partial A_z}{\partial x}, \frac{\partial A_y}{\partial t}, \frac{\partial A_z}{\partial t}) \qquad (5.45)$$

Using the differencing of Eqs. (5.31-5.32) and (5.35-5.36), Eqs. (5.44-5.45) become a tridiagonal system of coupled equations:

$$\mathbf{A}_I \cdot \vec{X}_{I-1} + \mathbf{B}_I \cdot \vec{X}_I + \mathbf{C}_I \cdot \vec{X}_{I+1} = \vec{D}_I \qquad (5.46)$$

where

$$\vec{X}_I = \begin{pmatrix} A_{y,I}^{N+1} \\ A_{z,I}^{N+1} \end{pmatrix} \qquad (5.47)$$

The matrices $\mathbf{A}$, $\mathbf{B}$, $\mathbf{C}$ are of the general form

$$\mathbf{Z} = \begin{pmatrix} z_1 & z_2 \\ -z_2 & z_1 \end{pmatrix} \tag{5.48}$$

with

$$a_1 = 1 - \delta a_2 \tag{5.49}$$

$$a_2 = -\frac{n_i \Delta x V_{ix}}{2 B_x (1 + \delta^2)} \tag{5.50}$$

$$b_1 = -2 - \delta b_2 \tag{5.51}$$

$$b_2 = \frac{n_i \Delta x^2}{B_x (1 + \delta^2) \Delta t} \tag{5.52}$$

$$c_1 = 1 - \delta c_2 \tag{5.53}$$

$$c_2 = -a_2 \tag{5.54}$$

$\vec{D}$ is given by

$$\vec{D} = -\frac{n_i \Delta x^2}{1 + \delta^2} \begin{pmatrix} V'_{iy} + \delta V'_{iz} - (A_{z,I} - \delta A_{y,I})/B_x \Delta t \\ V'_{iz} - \delta V'_{iy} + (A_{y,I} + \delta A_{z,I})/B_x \Delta t \end{pmatrix} \tag{5.55}$$

where

$$V'_{iy} = V_{iy} - V_{ix} B_{yc}/B_x \tag{5.56}$$

and

$$V'_{iz} = V_{iz} - V_{ix} B_{zc}/B_x \tag{5.57}$$

In the case of periodic boundary conditions considered here the set of equations (5.46) is easily solved, assuming a solution of the form

$$\vec{X}_I = \mathbf{E}_I \cdot \vec{X}_{I+1} + \vec{F}_I + \mathbf{G}_I \cdot \vec{X}_{NX1} \quad I = 1, 2, \ldots NX1 \tag{5.58}$$

(The case of fixed boundaries is somewhat easier; see Winske and Leroy (1984b) for details.) Substituting this solution for $\vec{X}_{I-1}$ into (5.46) yields

$$\begin{aligned} \vec{X}_I = &\ (\mathbf{A}_I \cdot \mathbf{E}_{I-1} + \mathbf{B}_I)^{-1} \\ &\cdot (-\mathbf{C}_I \cdot \vec{X}_{I+1} + \vec{D}_I - \mathbf{A}_I \cdot \vec{F}_{I-1} - \mathbf{A}_I \cdot \mathbf{G}_{I-1} \cdot \vec{X}_{NX1}) \end{aligned} \tag{5.59}$$

which is of the form (5.58) with

$$\mathbf{E}_I = -(\mathbf{A}_I \cdot \mathbf{E}_{I-1} + \mathbf{B}_I)^{-1} \cdot \mathbf{C}_I \tag{5.60}$$

$$\vec{F}_I = (\mathbf{A}_I \cdot \mathbf{E}_{I-1} + \mathbf{B}_I)^{-1} \cdot (\vec{D}_I - \mathbf{A}_I \cdot \vec{F}_{I-1}) \tag{5.61}$$

$$\mathbf{G}_I = -(\mathbf{A}_I \cdot \mathbf{E}_{I-1} + \mathbf{B}_I)^{-1} \cdot \mathbf{A}_I \cdot \mathbf{G}_{I-1} \tag{5.62}$$

Because all the $\mathbf{A}_I$, $\mathbf{B}_I$, $\mathbf{C}_I$, $\vec{D}_I$ are known, the $\mathbf{E}_I$, $\vec{F}_I$, $\mathbf{G}_I$ ($I = 3, ...NX1$) are easily computed if $\mathbf{E}_2$, $\vec{F}_2$, $\mathbf{G}_2$ are known to start the process. This is done using the boundary conditions; for example, in a periodic system

$$\vec{X}_1 \;=\; \vec{X}_{NX1} \tag{5.63}$$

and

$$\vec{X}_2 \;=\; \vec{X}_{NX2} \tag{5.64}$$

so that (5.46) for $I = 2$ becomes

$$\mathbf{A}_2 \cdot \vec{X}_1 + \mathbf{B}_2 \cdot \vec{X}_2 + \mathbf{C}_2 \cdot \vec{X}_3 \;=\; \vec{D}_2 \tag{5.65}$$

or

$$\vec{X}_2 = -\mathbf{B}_2^{-1} \cdot \mathbf{C}_2 \cdot \vec{X}_3 + \mathbf{B}_2^{-1} \cdot \vec{D}_2 - \mathbf{B}_2^{-1} \cdot \mathbf{A}_2 \cdot \vec{X}_{NX1} \tag{5.66}$$

which is of the form (5.58), yielding

$$\mathbf{E}_2 \;=\; -\mathbf{B}_2^{-1} \cdot \mathbf{C}_2 \tag{5.67}$$

$$\vec{F}_2 \;=\; \mathbf{B}_2^{-1} \cdot \vec{D}_2 \tag{5.68}$$

$$\mathbf{G}_2 \;=\; -\mathbf{B}_2^{-1} \cdot \mathbf{A}_2 \tag{5.69}$$

It is also evident that (5.58) then yields all the $\vec{X}_I$, provided $\vec{X}_{NX2}$ (or $\vec{X}_{NX1}$) is known. A repeated use of (5.58), starting with $I = 2$, yields

$$\begin{aligned}
\vec{X}_2 \;=\;& \mathbf{E}_2 \cdot \vec{X}_3 + \vec{F}_2 + \mathbf{G}_2 \cdot \vec{X}_{NX1} \\
\;=\;& \mathbf{E}_2 \cdot (\mathbf{E}_3 \cdot \vec{X}_4 + \vec{F}_3 + \mathbf{G}_3 \cdot \vec{X}_{NX1}) + \vec{F}_2 + \mathbf{G}_2 \cdot \vec{X}_{NX1} \\
\;=\;& \mathbf{E}_2 \cdot \mathbf{E}_3 \cdot (\mathbf{E}_4 \cdot \vec{X}_5 + \vec{F}_4 + \mathbf{G}_4 \cdot \vec{X}_{NX1}) + \mathbf{E}_2 \cdot \vec{F}_3 + \vec{F}_2 \\
& + (\mathbf{E}_2 \cdot \mathbf{G}_3 \cdot + \mathbf{G}_2) \cdot \vec{X}_{NX1}
\end{aligned} \tag{5.70}$$

etc., which can be eventually written as

$$\vec{X}_2 \;=\; \mathbf{E}_c \cdot \vec{X}_{NX1} + \vec{F}_c + \mathbf{G}_c \cdot \vec{X}_{NX1} \tag{5.71}$$

where, evidently

$$\mathbf{E}_c \;=\; \mathbf{E}_2 \cdot \mathbf{E}_3 \cdot \mathbf{E}_4 \cdots \mathbf{E}_{NX} \tag{5.72}$$

$$\vec{F}_c \;=\; \vec{F}_2 + \mathbf{E}_2 \cdot \vec{F}_3 + \mathbf{E}_2 \cdot \mathbf{E}_3 \cdot \vec{F}_4 + \cdots + \mathbf{E}_2 \cdot \mathbf{E}_3 \cdots \vec{F}_{NX} \tag{5.73}$$

$$\mathbf{G}_c \;=\; \mathbf{G}_2 + \mathbf{E}_2 \cdot \mathbf{G}_3 + \mathbf{E}_2 \cdot \mathbf{E}_3 \cdot \mathbf{G}_4 + \cdots + \mathbf{E}_2 \cdot \mathbf{E}_3 \cdots \mathbf{G}_{NX} \tag{5.74}$$

Using (5.46) for $I = NX1$ then yields

$$\mathbf{A}_{NX1} \cdot \vec{X}_{NX} + \mathbf{B}_{NX1} \cdot \vec{X}_{NX1} + \mathbf{C}_{NX1} \cdot \vec{X}_{NX2} \;=\; \vec{D}_{NX1} \tag{5.75}$$

Using (5.58) to express $\vec{X}_{NX}$ in terms of $\vec{X}_{NX1}$ and (5.64) and (5.73) to express $\vec{X}_{NX2}$ in terms of $\vec{X}_{NX1}$ then yields

$$
\begin{aligned}
\vec{X}_{NX1} &= [\mathbf{A}_{NX1} \cdot (\mathbf{E}_{NX} + \mathbf{G}_{NX}) + \mathbf{B}_{NX1} + \mathbf{C}_{NX1} \cdot (\mathbf{E}_c + \mathbf{G}_c)]^{-1} \\
&\quad \cdot (\vec{D}_{NX1} - \mathbf{A}_{NX1} \cdot \vec{F}_{NX} - \mathbf{C}_{NX1} \cdot \vec{F}_c)
\end{aligned} \tag{5.76}
$$

which with (5.58) completes the solution of $\vec{X}_I = (A_{y,I}^{N+1}, A_{z,I}^{N+1})$.

We can then use Eqs. (5.31-5.32) and (5.35-5.36) to obtain B_y^{N+1}, B_z^{N+1}, E_y^{N+1}, E_z^{N+1}. With an assumed model for the electron pressure, the x component of (5.4) can then be solved for E_x:

$$
E_x = -(\vec{V}_e \times \vec{B})_x - \frac{1}{n_i} \frac{\partial P_e}{\partial x} \tag{5.77}
$$

with

$$
\vec{V}_e = \nabla^2 \vec{A}/n_i + \vec{V}_i \tag{5.78}
$$

This completes the solution of the field equations. One now continues the cycle by again moving the ions in the new fields and collecting the moments to then solve the field equations at the next time step.

5.2.5 Initialization

To complete the discussion of the mechanics of the hybrid code, we turn to how to get started: the initialization. We need to load the particles in both physical space as well as velocity space and to initialize the fields. The last part is easiest, because after all the particles are loaded, we can "move" them with $\Delta t = 0$ to collect the moments and solve the field equations at $t = 0$.

Loading the particles in space is also straightforward. For the problems to be considered in our simple test code, the initial densities are uniform and the particles are loaded uniformly in space

$$
x_p = \text{XMAX} \, \frac{I_{pj} - 1/2}{N_{pj}} \tag{5.79}
$$

where I_{pj} =particle number= $1, 2, ...N_{pj} \equiv$ total number of particles of species j. In general, of course, the initial density may be a function of x, $n_j(x)$. In this case if we define a function G_j

$$
G_j(x) = \int_o^x n_j(x')dx' \tag{5.80}
$$

we can invert the function

$$
\frac{G_j(x_p)}{G_j(XMAX)} = \frac{I_{pj} - 1/2}{N_{pj}} \tag{5.81}
$$

to find x_p for each I_{pj}. We can use any number of simulation particles to represent each ion species, multiplying the species density by some factor to represent the actual physical density. For example, we will find it useful later to use half the simulation particles to represent a very weak beam, $n_b \ll n_o$, with the other half for the denser background component.

In similar fashion we load the ions in velocity space by defining a loading function $R_j(\vec{v})$ in terms of the velocity distribution $F_j(\vec{v})$ [e.g., Aldrich, 1985]. This can be done component by component. However, in the special case of gyrotropic or isotropic distributions it is often easier to do two components together, i.e.,

$$v'_y = v'_\perp \cos\phi \tag{5.82}$$

$$v'_z = v'_\perp \sin\phi \tag{5.83}$$

where ϕ is a random angle $0 \leq \phi \leq 2\pi$. The magnitude $v_\perp$ is obtained by inverting

$$R_j(v'_\perp) = \frac{\int_0^{v'_\perp} F_j(v_\perp)v_\perp dv_\perp}{\int_0^\infty F_j(v_\perp)v_\perp dv_\perp} \tag{5.84}$$

For example, if $F_j(\vec{v})$ is Maxwellian

$$R_j(v'_\perp) = 1 - \exp(-v'^2_\perp/v^2_j) \tag{5.85}$$

which is easily inverted to obtain $v_\perp$. Evidently, $0 < R_j < 1$ and choosing R_j to be a random number between 0 and 1 then gives a random $v_\perp$ and hence a random loading to v'_y and v'_z. One can also do the same with v'_x (throwing away the second velocity component.) Here, v'_y and v'_z are perpendicular to the magnetic field direction, while v'_x is parallel to $\vec{B}_o$, which may not be along the x axis. We then rotate the particle velocities v'_x, v'_y, v'_z to v_x, v_y, v_z in the usual manner. This method is readily extended to include a nonrandom drift or other forms of the distribution function. It is also possible to weigh the particles differently in order to load them preferentially in some regions of velocity space (e.g., Burgess [1987]).

5.2.6   Diagnostics

Lastly, a discussion of a simulation code would not be complete without the diagnostics, whereby the outputs of the calculation are expressed in a form that can be related to the physics. In the version of the code discussed here, there are three kinds of output. First, during the run various quantities are plotted out and saved in a PLOT file. These include phase space $(x - v_x,\ x - v_y,\ x - v_z)$ plots of the various ion species at specified time intervals. Also plotted are profiles in x of the magnetic fields and the density of each ion species. Generally, these profiles are plotted with scales that adjust to the minimum and maximum value displayed in order to insure that all important effects (as well as potential

problems) are visible. Plots with fixed scales, suitable for publication, can generally be produced via a postprocessor later.

Second, at specified intervals we calculate the velocity and temperature (each component separately) and the energy of each ion species. We also calculate the energy in the magnetic and electric fields, the total particle energy, and the total energy in the system. These quantities are written into an OUTPUT file. In addition to looking at the numbers, one can also obtain plots during the run of some of these quantities.

Thirdly, the full array of NX values of the transverse components of the magnetic field (B_y, B_z) are written into files BYS and BZS, respectively, every few time steps. These files can then be postprocessed to generate at desired time intervals such field quantities as profiles of B_y, B_z, $|B| = (B_y^2 + B_z^2)^{1/2}$ and $\phi = \tan^{-1} B_z/B_y$ with suitably defined, fixed scales. In addition, Fourier spectra of these quantities can be produced as well as space-time plots of the entire run (examples shown later). Also, the magnetic field can be decomposed into waves with positive and negative helical parts [Terasawa *et al.*, 1986]. Profiles, Fourier spectra, and space-time plots of these separate helical components can also be generated. Similar diagnostics can be developed for the density as well as the electric fields, if one chooses to save these quantities as well. Many of these displays vary with the individual problem, the preferences of the simulator, *etc.* Thus, we leave this part of the diagnostics to the designs of the reader, but some relevant examples will be shown later.

5.3 Simple Applications

In this section we consider some elementary, but nevertheless interesting problems that can be studied with a 1-D hybrid code. We begin with the resonant electromagnetic ion/ion instability that is driven by a low density field aligned ion beam moving with respect to the background ions at a velocity large compared to the Alfven speed. This instability was briefly discussed in Section 4.1 in relation to the ion foreshock. The physical mechanism of the instability and its properties inferred from linear theory are first described. We then go through the reasoning needed to set up the simulation and show some representative results from an actual calculation, both from the PLOT file generated during the run as well as some plots obtained from a postprocessor. We then compare the output to the predictions of linear theory and briefly describe some nonlinear effects. We also discuss some simple numerical tests that are useful to assess the accuracy of the results and their sensitivity to various numerical parameters. Next, we discuss other sample problems, which include the nonresonant ion/ion instability that occurs at higher beam density [Gary *et al.*, 1981; Sentman *et al.*, 1981; Winske and Leroy, 1984a] and the electromagnetic ion cyclotron beam anisotropy instability [Gendrin *et al.*, 1984; Gary and Schriver, 1987] that is excited when there is a temperature anisotropy ($T_{b\perp}/T_{b\parallel} > 1$) in

the beam. We then consider how to modify the code to change the initial conditions (to study other instabilities), to include injection of particles (to simulate active experiments and comets), and how to switch the boundary conditions (to generate collisionless shocks). These types of problems have been well studied; here we outline the changes that are needed in the code and cite the appropriate references to direct the interested reader.

5.3.1 Resonant electromagnetic ion/ion instability

Let us assume there is a weak (density $n_b \ll n_o$) ion beam drifting relative to a background ion population (density n_i, $n_o = n_b + n_i$) along a uniform magnetic field ($B_o \hat{x}$) with relative velocity $V_b \gg v_A$ (v_A =Alfven speed= $B_o(4\pi n_o m_o)^{-1/2}$). For simplicity, we take both ion species as protons (see Winske and Gary [1986] for the more general case). We assume that there is no net current in the system and take the charge neutralizing electron background at rest. Relative to the electrons the beam velocity is thus $V_b = (1 - n_b/n_o)V_b \hat{x}$, while the background ions drift at $V_i = -(n_b/n_o)V_b \hat{x}$. Assuming waves with complex frequency $\omega = \omega_r + i\gamma$ and wavenumber k, the linear dispersion equation for electromagnetic waves propagating along the background magnetic field in the cold plasma limit is [Scharer and Trivelpiece, 1967]

$$\omega^2 - c^2 k^2 - \sum_j \frac{\omega_j^2(\omega - kV_j)}{\omega - kV_j \pm \Omega_j} = 0 \tag{5.86}$$

where $j = e$ (electrons), b (beam ions) or i (background ions), $\omega_j^2 = 4\pi n_j e^2/m_j$ (with $n_e = n_o = n_b + n_i$), $\Omega_j = e_j B_o/m_j c$ ($\Omega_b = \Omega_i$ for $m_b = m_i = m_o$), and the +(-) sign refers to right (left) hand polarized waves. For right hand polarized waves propagating in the direction of the beam, the resonant electromagnetic ion/ion instability occurs for

$$\omega - kV_b + \Omega_i \simeq 0 \tag{5.87}$$

i.e., the beam ions are in cyclotron resonance with the waves. Note that in the reference frame of the beam the waves are left hand polarized (ion cyclotron) waves, but in the electron frame they are right hand polarized.

The dispersion equation (5.86) can be solved analytically for $n_b/n_o \ll 1$, $V_b/v_A \gg 1$ [Kovner, 1961; Quest, 1988] to yield

$$[(\gamma/\Omega_i)^2 + (v_A/V_b)^2]^{1/2}(\gamma/\Omega_i)^2 \simeq n_b/2n_o \tag{5.88}$$

For very weak beams $\gamma \simeq 0$ and

$$\gamma \simeq (n_b/2n_o)^{1/2}(V_b/v_A)^{1/2}\Omega_i \tag{5.89}$$
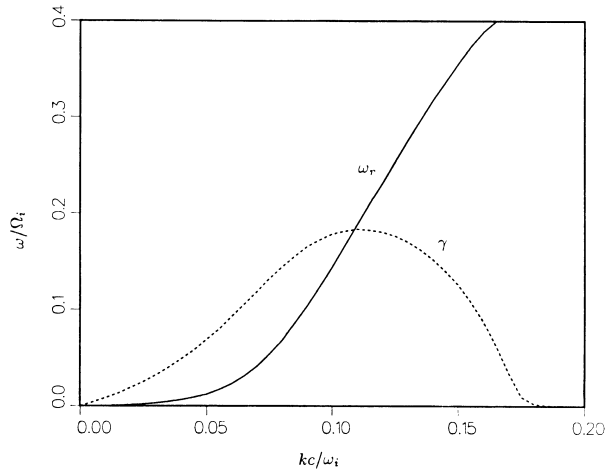
Figure 5.3: Results from linear theory for the resonant electromagnetic ion/ion instability ($n_b/n_o = 0.015$, $V_b/v_A = 10$, $\beta_b = \beta_i = \beta_e = 1$), showing ω_r (solid line) and γ (dashed line) versus k.

But for beam densities of the order of a few per cent (like the foreshock), $\gamma/\Omega_i > v_A/V_b$ and

$$\gamma \simeq (n_b/2n_o)^{1/3}\Omega_i \qquad (5.90)$$

[Winske, and Leroy, 1984a]. Numerical solutions of (5.86) verify that for beam velocities somewhat above threshold, the growth rate maximized over wavenumber is indeed independent of V_b (cf. Figure 4, Winske and Leroy [1984a]).

The linear and nonlinear properties of the instability have been thoroughly studied via simulation [Winske and Leroy, 1984a; Hoshino and Terasawa, 1985; Gary et al., 1986; Terasawa, 1988; Zachary et al, 1989; Omidi and Winske, 1990; Akimoto and Winske, 1990]. Thus, it is a good test problem for illustrating the use of hybrid code techniques. As in Winske and Leroy [1984a], we take the beam velocity relative to the background ions to be $10v_A$, the plasma beta of each species to be unity ($\beta_j = 8\pi n_o T_j/B_o^2 = 1$), and the beam density ratio, $n_b/n_o = 0.015$.

With these parameters a numerical solution of the complete electromagnetic dispersion equation [e.g., Gary et al. 1981], rather than of the simplified version (5.86), yields the growth rate (dashed curve in Figure 5.3) and real frequency (solid curve) as a function of wavenumber, kc/ω_i. The growth rate peaks at $kc/\omega_i \simeq 0.12$ with $\gamma_{max}/\Omega_i \simeq \omega_r/\Omega_i \simeq 0.2$, and the unstable modes persist out only to $kc/\omega_i \simeq 0.18$. Thus, the wavelength of the dominant unstable

mode is about $50c/\omega_i$. Because we wish to have the system contain at least four wavelengths of the most unstable mode, the system length should be $\geq 200c/\omega_i$. Furthermore, to simplify the use of the fast Fourier transform routine, it is most convenient to take NX to be a power of 2. We thus choose $NX = 128$ and $HX = 2c/\omega_i$ so that $XMAX = 256c/\omega_i \simeq 5$ wavelengths of the dominant linear mode, which allows plenty of room for possible wave-wave interactions and enough cells to well resolve the dominant modes. The number of particles per cell should be large enough to give good statistics, yet not too many to make the run time excessive. With $NX = 128$ a reasonable number is 80 particles per cell, *i.e.*, 10240 total particles in the system, as shown in the next subsection. Because the instability is driven by a cyclotron resonance with the beam ions, we represent the beam species with half of the simulation particles, the background ions with the other half. The simulation, like the linear theory, is done in the frame where the electrons are at rest, although this is not necessary. We could just as easily do the calculation in the background or beam ion frame. There are, however, some numerical pitfalls and limitations to be aware of. These are discussed in the next subsection.

In similar fashion we see from Figure 5.3 that the maximum growth rate is $\gamma_{max}/\Omega_i \simeq 0.2$. A useful rule of thumb is that the run time should be at least $10\gamma_{max}^{-1}$, *i.e.*, $50\Omega_i^{-1}$. The time step should be small enough so that the particles do not traverse more than one cell per time step ($V_{max}\Delta t < HX$). With $V_{max} \sim V_b = 10v_A$ and $HX = 2c/\omega_i$, taking $\Omega_i\Delta t = 0.05$ satisfies both conditions. We thus choose $NTIMES =$ number of time steps in the run $=2000$ (*i.e.*, $\Omega_i t_{max} = 100$). It will be useful to generate pictures every 200 time steps ($10\Omega_i^{-1}$), store the fields every 20 time steps and write out the moments and energies every 40 time steps. As mentioned before, in the hybrid code ω_i/Ω_i is arbitrary; we thus take $\omega_i/\Omega_i = 10^4$.

Some results from the run are shown in the next series of figures. We show representative panels from the PLOT file generated during the run at several times ($\Omega_i t = 20$, 40, 60): $x - v_x$ and $x - v_y$ phase space for the beam ions, the beam density (normalized to its initial value), B_y (normalized to B_o), and phase angle $\phi = \tan^{-1} B_z/B_y$. By $\Omega_i t = 20$ (Figure 5.4) the instability has begun to develop. There are transverse waves in B_y of modest amplitude ($B_y/B_o \simeq 0.2$) and corresponding oscillations in the beam v_y velocity that are evidently out of phase with B_y by about 90°. Note that the dominant mode is $m = 5$, consistent with linear theory, although there are evidently many other waves, some much shorter in wavelength that are mostly noise. The plot of ϕ shows a left hand sense of rotation as one proceeds towards positive x (the direction of $\vec{B}_o$ and $\vec{k}$); this corresponds to positive helicity [Gary, 1986]. Some fluctuations have begun to develop in n_b ($\delta n_b/n_b \sim 0.3$) and slowing of the ions in v_x is beginning to occur. At $\Omega_i t = 40$ (Figure 5.5), the wave amplitudes are much larger ($B_y/B_o \sim 0.9$) and because of the fast growth of the dominant modes, the waveforms have become more sinusoidal (note that the scales on
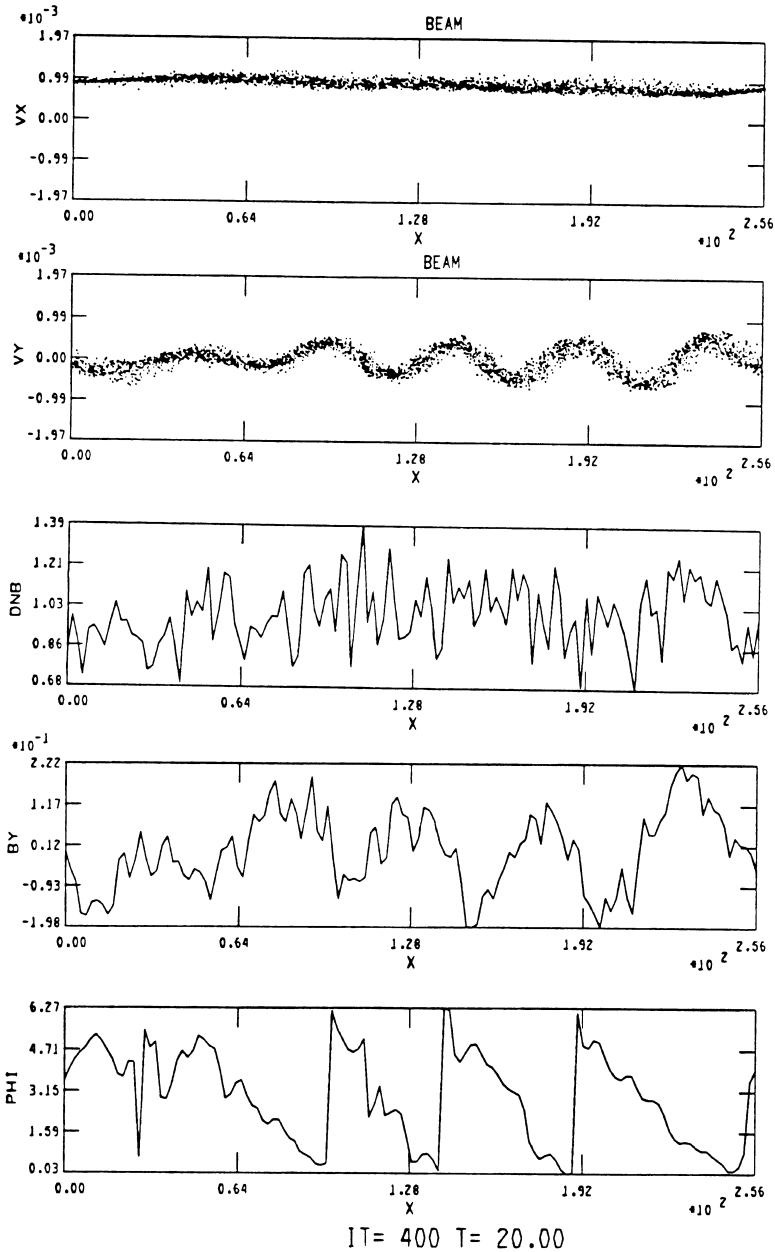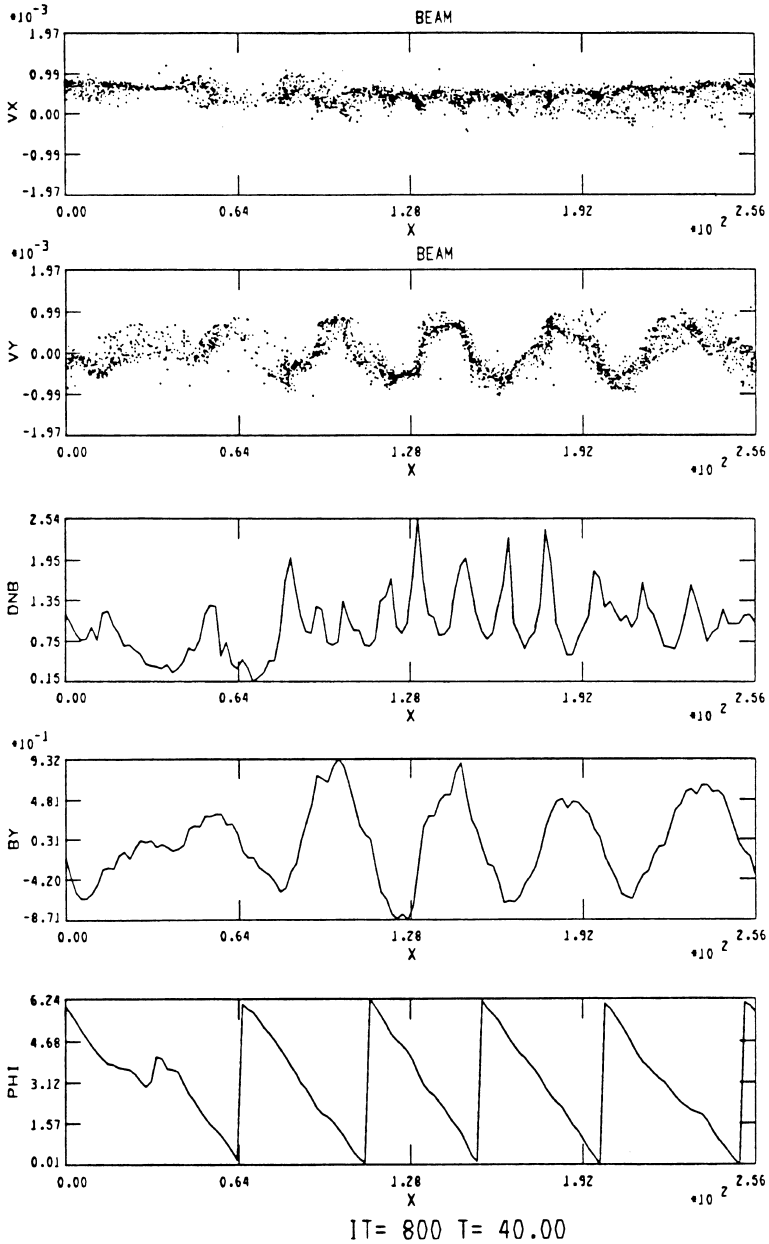
Figure 5.4: Results of simulation of the resonant instability at $\Omega_i t = 20$: $x - v_x$ and $x - v_y$ phase space for the beam ions and profiles of the beam density, B_y, and $\phi = \tan^{-1} B_z/B_y$.

Figure 5.5: Corresponding simulation results at $\Omega_i t = 40$.

the plots have changed), and the helicity is very well defined. The beam ions have started to become scattered in v_y, and the beam has begun to be spatially bunched, heated, and slowed in v_x. The corresponding fluctuations in the beam are very large ($\delta n_b/n_b \sim 2$). By $\Omega_i t = 60$ (Figure 5.6), the beam has been thermalized with a remnant of smaller amplitude, more irregular magnetic field and density fluctuations. Further information about the waves can also be obtained. Figure 5.7, for example, shows Fourier spectra of B_y at various times in the run. While mode 5 dominates early, consistent with linear theory, and remains large throughout the run, at later times mode 6 dominates and the overall spectrum is broadened and more complex.

Also generated during the run are plots of time histories of various quantities, some of which are shown in Figure 5.8. Displayed are histories of the fluctuating magnetic field energy density, $\delta B^2/B_o^2$, the beam velocity, and parallel and perpendicular temperatures (normalized to their initial values). We see the growth of the fluctuations, which peak at $\Omega_i t \sim 35$, and then decay to a lower level. The beam velocity drops as the waves grow and the beam is heated first in the perpendicular direction and more slowly in the parallel direction. These changes correlate well with second order theory [Winske and Leroy, 1984a].

Other information about the fields can be obtained from the magnetic fields stored during the run in the BYS BZS files, which can be analyzed after the run by writing a simple postprocessor. A very useful type of display is a time sequence of magnetic field profiles stacked upon each other. Figure 5.9 displays such space-time profiles of the B_y component of the decomposition of the transverse waves into their helical parts [Terasawa *et al.*, 1986; Miller *et al.*, 1991], as discussed in Appendix B. The left panel corresponds to the positive helicity part (left hand sense of rotation in space in the direction of $\vec{k}$ and $\vec{B}_o$), the right panel is the negative helicity part. For the positive helicity component waves traveling to the right are right hand polarized, while waves traveling to the left are left hand polarized. Similarly, in the right hand panel waves traveling to the right are left hand polarized, those moving to the left are right hand polarized. Note that a Galilean shift in the frame of reference of the simulation (*i.e.*, from the electron frame to the beam frame) does not change the helicity, although the polarization may change. Similarly, if we reverse the direction of the beam (or of the ambient magnetic field), the helicity changes, although the polarization of the waves will not. In the present case positive helicity waves propagating to the right predominate, as predicted by linear theory, with just low amplitude noise in the other helicity component. It can also be seen that some of the positive helicity waves seem to split into two parts, with one wave front then moving to the left at about the same speed as the other part that is moving to the right. From the space-time evolution of the phase fronts one can infer a real frequency, $\omega_r \simeq 0.2\Omega_i$, consistent with Figure 5.3 [one can do this more carefully by constructing a similar plot for each Fourier component to obtain $\omega_r(k)$]. Similarly, to obtain growth rates one can plot time histories

IT=1200 T= 60.00
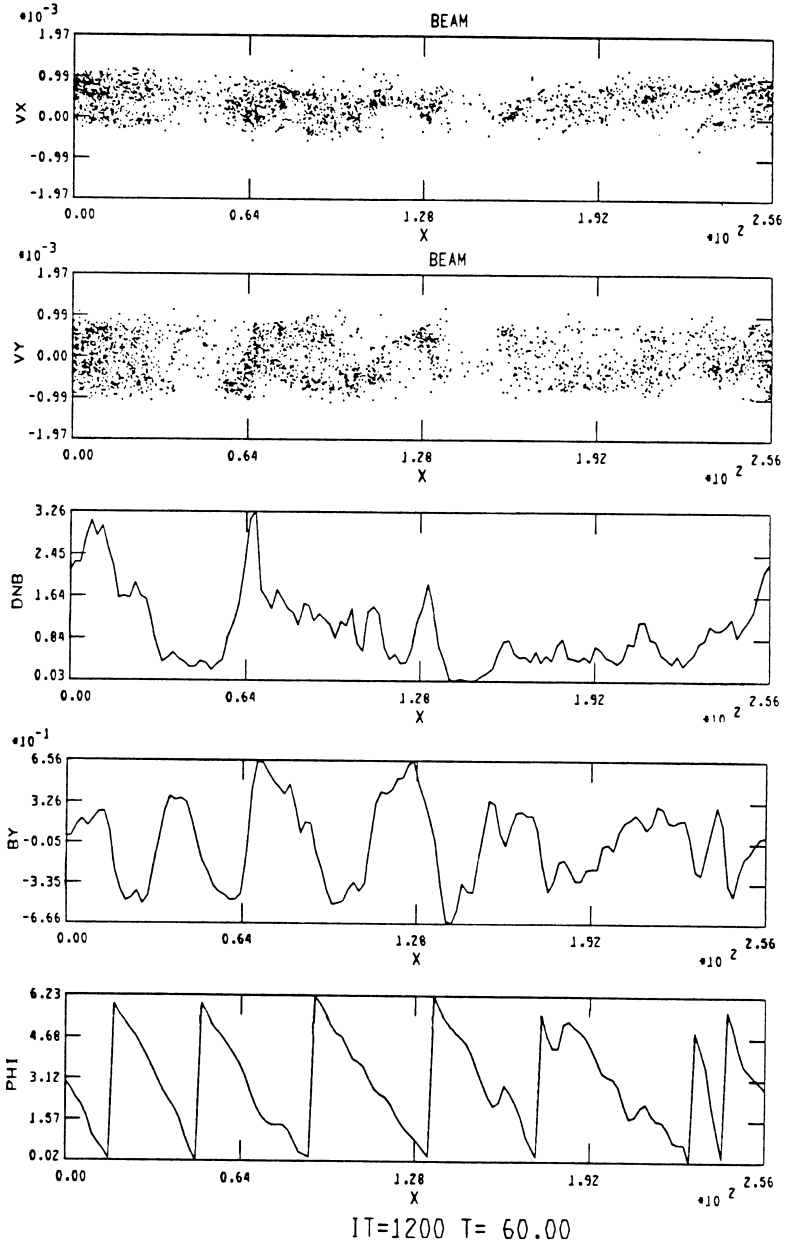
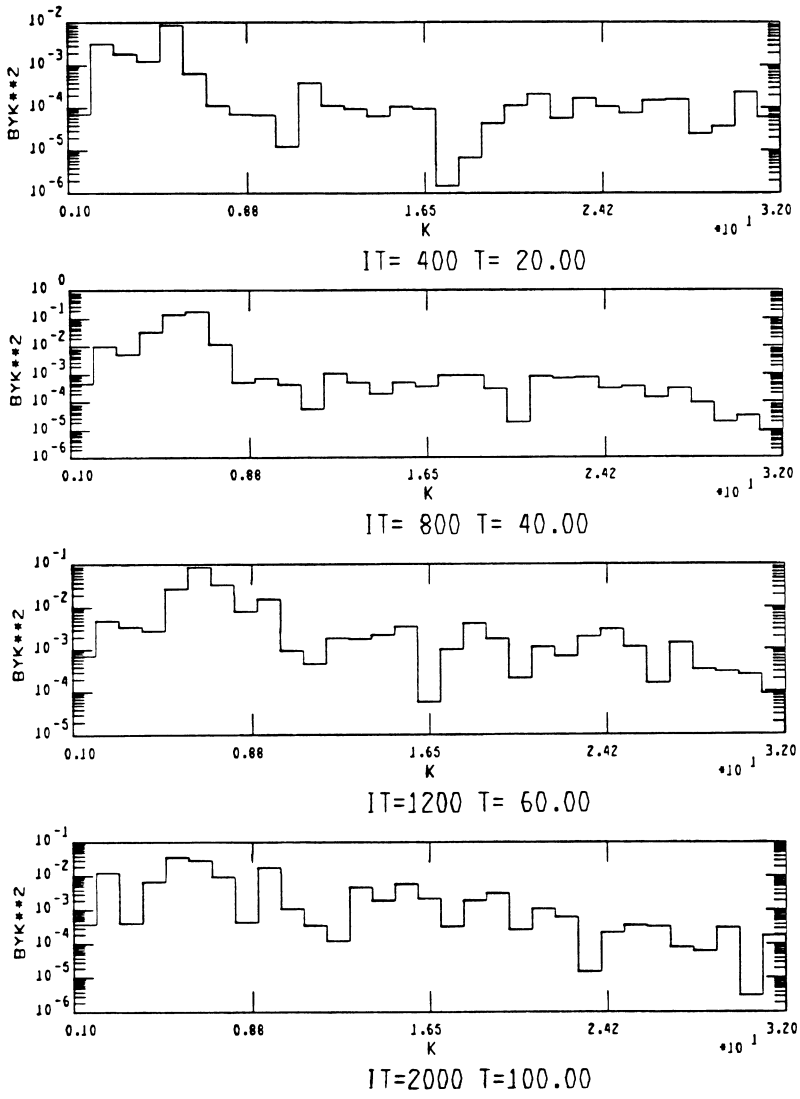Figure 5.6: Corresponding simulation results at $\Omega_i t = 60$.

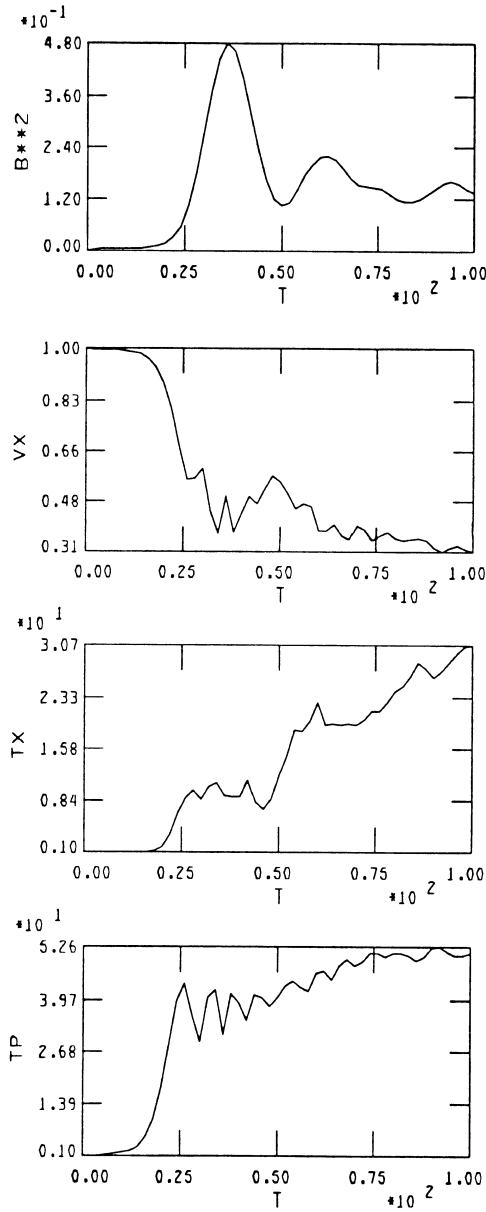Figure 5.7: Fourier spectral density of B_y at various times.

Figure 5.8:   Time histories from same run: magnetic field energy density $\delta B^2/B_o^2$, beam velocity V_b and parallel and perpendicular beam temperatures (normalized to their values at $t = 0$).
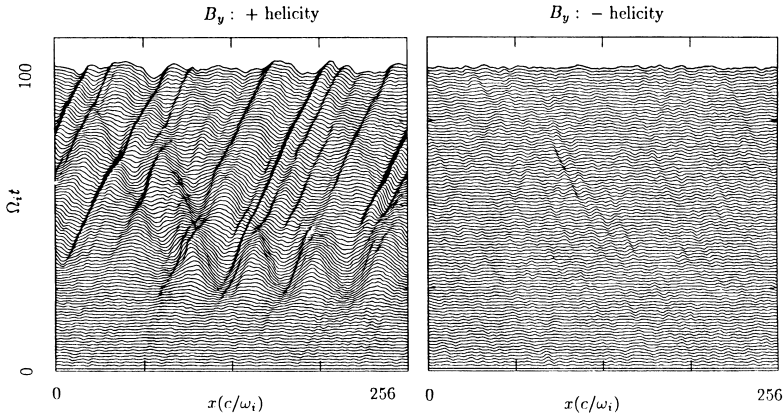
Figure 5.9: Space-time profiles of B_y: [left panel] positive helicity component; [right panel] negative helicity component.

of the Fourier modes of the separate helical components. For example, Figure 5.10 shows such histories of the first six Fourier modes of B_y^+, from which $\gamma_{m=5} \simeq 0.2\Omega_i$ can be obtained, again in good agreement with linear analysis.

Thus, from more specialized diagnostics additional information about the instability is easily obtained. We have, however, only briefly discussed some of the interesting physical processes that occur during the evolution of the instability. To see such effects better, even more detailed diagnostics are needed; the interested reader is encouraged to read the extended list of references cited earlier. For example, as the instability develops, the beam ions become gyrophase bunched. This is suggested by the correlation of the $x - v_y$ and B_y plots. However, to see the phase bunching in more detail, one needs to plot the phase of the waves $\tan \phi = B_z/B_y$ and that of the beam ions $\tan \chi = v_z/v_y$ together (e.g., Figure 5.6 of Hoshino and Terasawa [1985]). At early times there is a well defined difference between these two phase angles, which disappears as the beam ions give up energy to the waves. The nonlinear consequences of this gyrophase bunching include the generation of density pulses (e.g., Figure 5.5) [Terasawa, 1988] and corresponding magnetic field pulses ("pulsations") [Akimoto and Winske, 1990]. The nonlinear behavior of the instability also involves complex wave-wave interactions that depend to some degree on the beam parameters [Terasawa, 1988] as well as the generation and interaction of soliton-like structures [Akimoto and Winske, 1990].
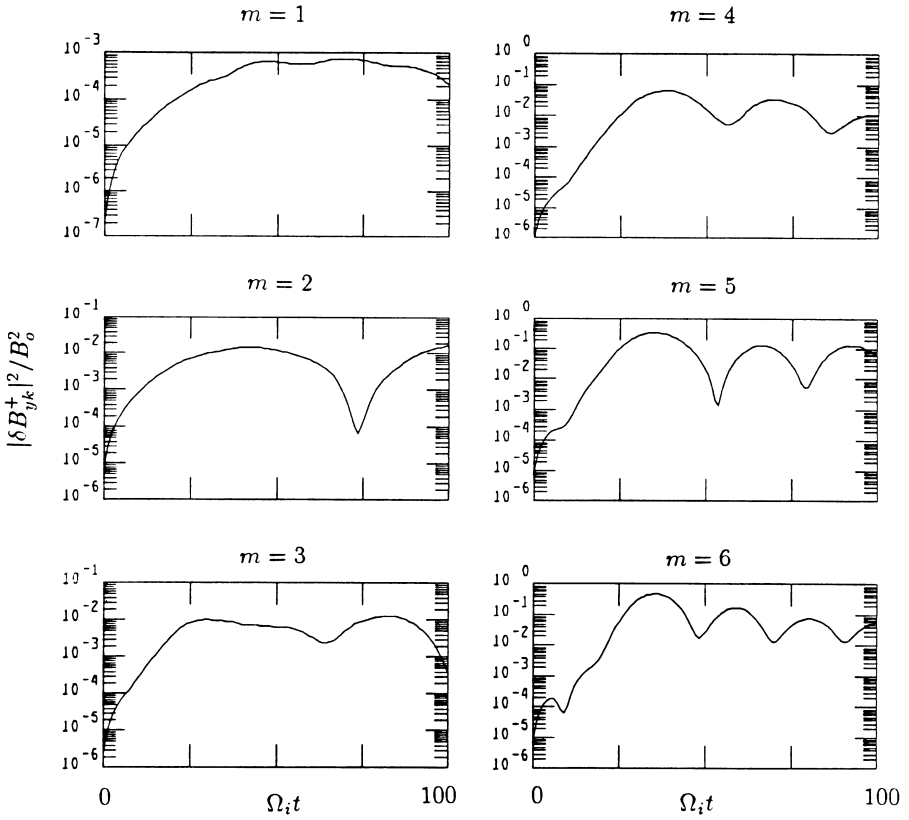
Figure 5.10: Time histories of several Fourier modes (positive helicity part), $|B^+_{yk}|^2$.

5.3.2   Numerical checks

Having carried out a successful simulation of the resonant electromagnetic ion/ion instability, using linear theory as a guide to verify properties of the mode, we turn to the question of the accuracy of the calculation, *i.e.*, how sensitive are the results to the numerics. We briefly discuss a few simple tests, which are useful in differentiating between physics and numerics, on this same sample problem. We leave other checks as additional exercises for the reader. The degree to which such tests are necessary depend to some degree on the problem and the familiarity of the user with the code.

   One simple numerical test is to vary the number of simulation macroparticles. As we show in detail later, increasing the number of particles per cell reduces the noise level and usually allows an instability to grow up out of the noise more readily. However, there is a tradeoff, as more particles increases the run time, and hence the expense of the calculation. We consider the resonant electromagnetic ion/ion instability with the same physical parameters as used in the run shown in Figures 5.4-5.10. We also keep the number of cells, the size of the time step, and the number of time steps fixed to their previous values. Some results are shown in the next three figures. The previous run, which had 10240 macroparticles (80 particles/cell, half to represent each ion species) is labelled in the figures as (b). We also consider 160 particles/cell (a) as well as 40 (c) and 20 (d) particles/cell. Figure 5.11 shows the magnetic field energy density as a function of time for these runs (the other two runs, denoted (e) and (f), will be discussed later). In each case there is a well define (exponential) increase of the fluctuations to a maximum, followed by a rapid decay to a smaller level that tends to oscillate in time. Generally, there is a decrease in the peak fluctuation level as the particle number decreases and an increase in the level of wave activity at early times before the instability begins to grow. (The somewhat higher than expected peak fluctuation level in the 40 particle/cell case is within the expected case-to-case variation, as shown later.) The time of saturation of the instability also decreases slightly as the particle/cell number is reduced, as the waves grow from larger initial values.

   Histograms of the spectral density of B_y at $\Omega_i t = 30$ for these same runs are displayed in Figure 5.12. With 160 particles/cell there is a very clean, sharply peaked spectrum, as one would expect from linear theory (Figure 5.3). With smaller particle numbers, the spectrum is less nicely shaped: modes 5 and 6 are about the same amplitude in (b) and modes 3-6 are all large in (c). Beyond mode $m \simeq 8$ the spectrum is essentially flat (these modes are stable according to linear theory). As expected, the fluctuation level in these short wavelength modes decreases as the number of particles per cell increases. Figure 5.13 shows B_y profiles in x at the same time. Again, one sees mode $m \simeq 5$ dominates, and an increase in the overall magnitude of the waves at this time and in the amount of short wavelength noise at lower particle/cell number. The profiles
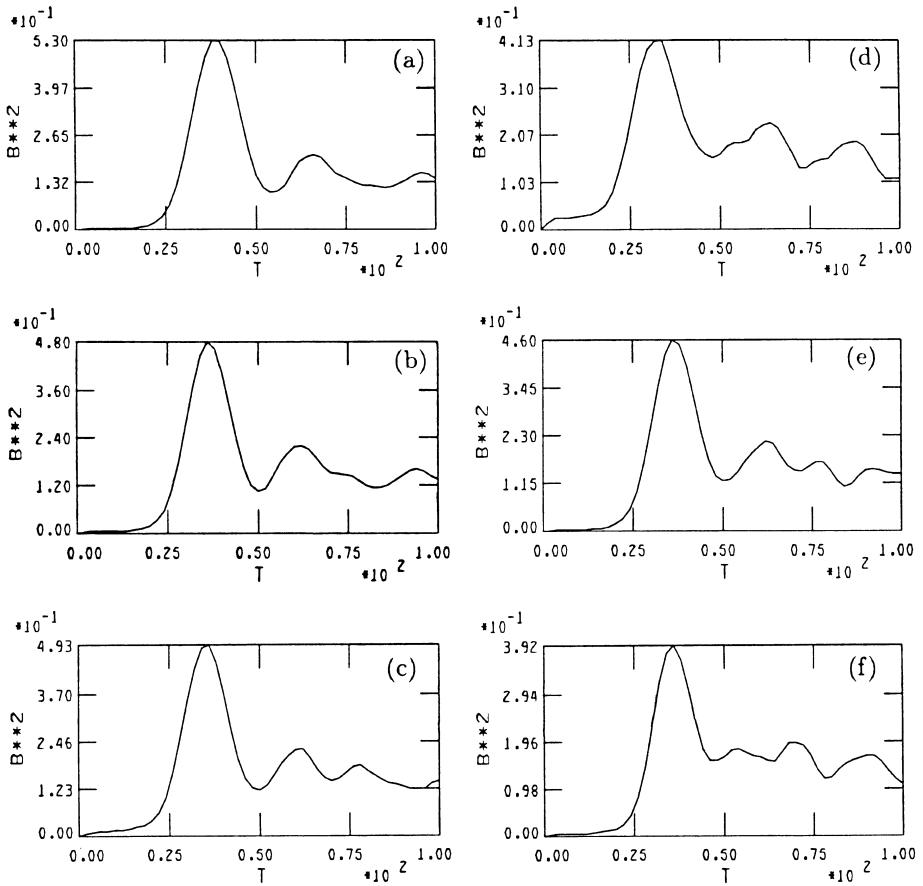
Figure 5.11: Time history of the magnetic field energy density $(\delta B^2/B_o^2)$ for the resonant electromagnetic ion/ion instability (same physical parameters as in Figure 5.3), varying numerical parameters: (a) 160 particles/cell, (b) 80 particles/cell, (c) 40 particles/cell, (d) 20 particles/cell, (e) exchanging beam and background components, and (f) smoothing the source terms in the 80 particle/cell run. (In each case half of the simulation particles represent each ion species.)
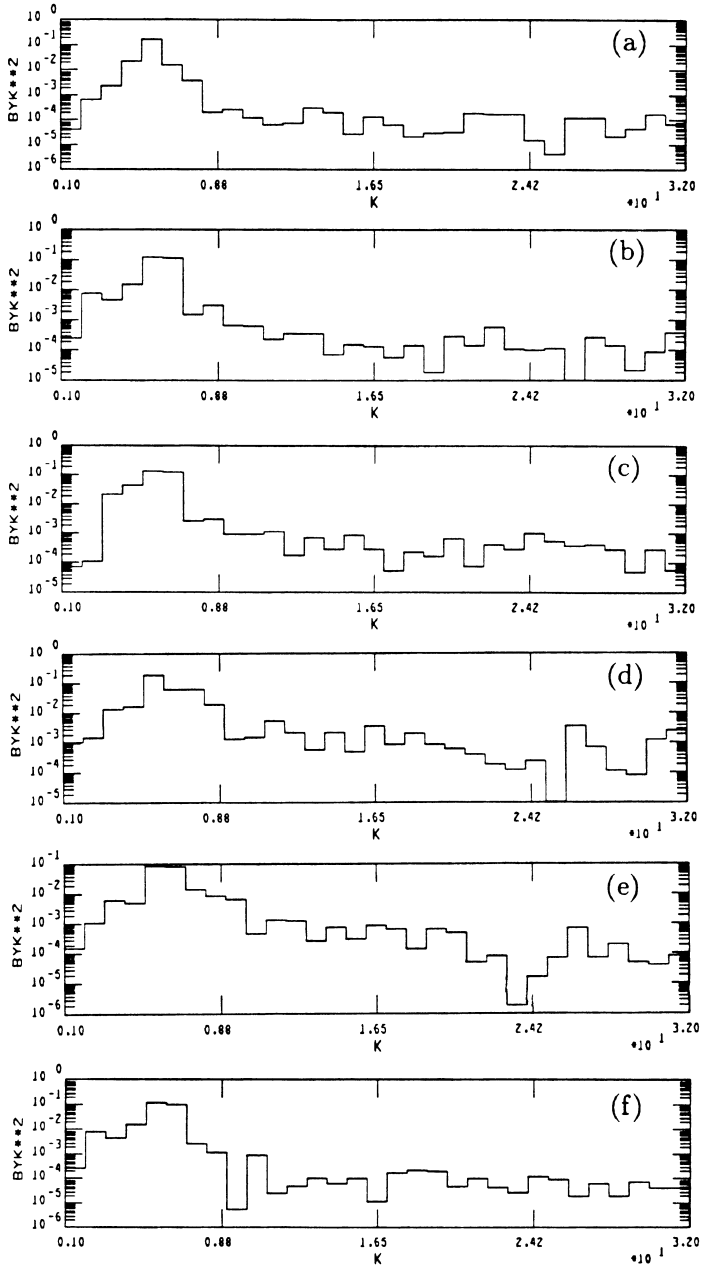
Figure 5.12: Fourier spectral density of B_y at $\Omega_i t = 30$ for the same runs as the previous figure.
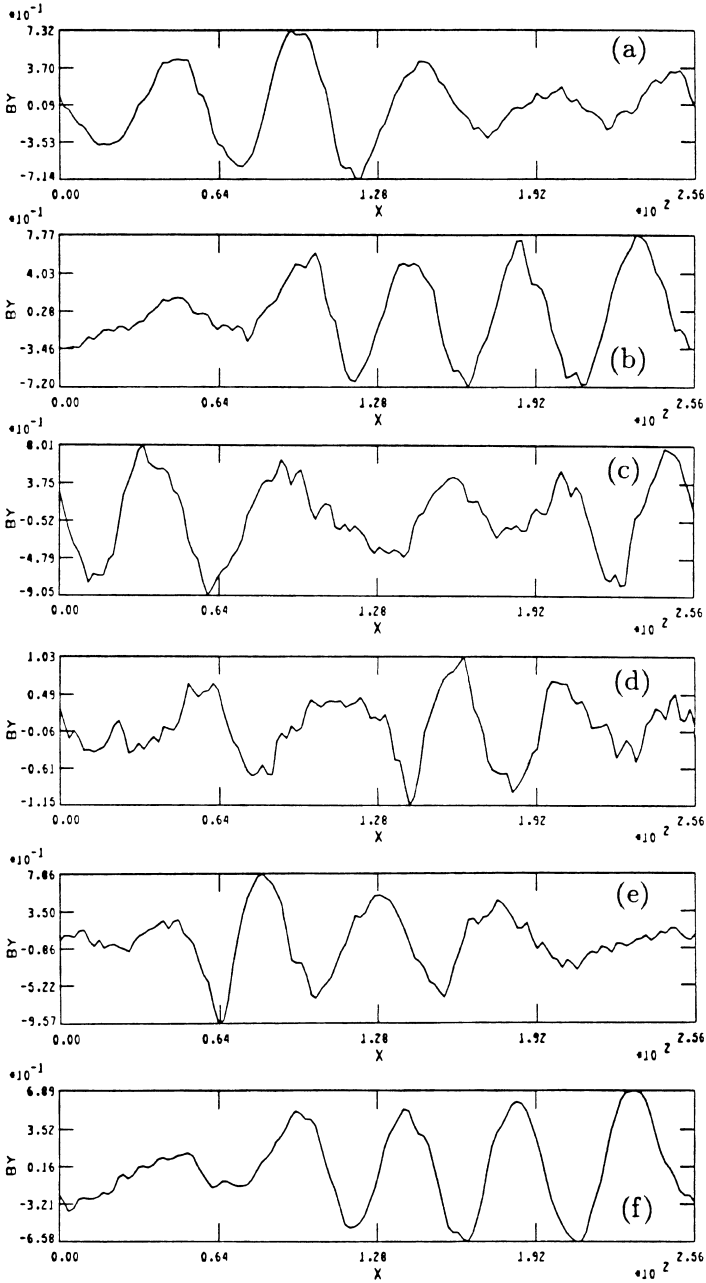
Figure 5.13: Profiles of B_y versus x for the same runs as in Figure 5.11.

also demonstrate the considerable variation in the wave pattern from run to run.

Another simple test is to exchange the two ion components (*i.e.*, make species #1 the background, #2 the beam). This run, using 80 particles/cell, is shown in panel (e) in Figures 5.11-5.13. Compared to its counterpart (b), we see slight differences ($\sim 4\%$) in the peak fluctuation level, some variation in the spectral density, and significant differences in the shape of the B_y profile (with very similar wave levels). These differences are evidently due to changing the seed of the random number generator used in the initialization of the particle velocities.

One can also reduce the high frequency noise in the simulation by smoothing the ion density and currents. Again using 80 particles/cell, a run with such smoothing has been carried out and is plotted in Figures 5.11-5.13 in panels (f). As seen in Figure 5.12, there is some reduction in the high frequency noise, as described quantitatively later, resulting in a smoother profile (Figure 5.13). The most noticeable effect is a significant reduction in the saturation level of the waves (Figure 5.11). While in this problem smoothing does not appear to be useful, in other situations (e.g., shocks) it can be very helpful in removing unwanted high frequency waves.

We next consider the related issue of the effect of the inherent noise in the simulation on the ions. We consider the same test run, with the beam density set to zero (*i.e.*, DNSPEC(1)=0 in the INPUT file). In this case there is no instability and the beam ions are essentially test particles. We again consider 80 particles/cell, but since the beam ions don't contribute here, we actually just have 40 (background) ions/cell. Figure 5.14 shows v_y-x phase space for both the beam and background ions at $\Omega_i t = 0$ and $\Omega_i t = 50$. There is negligible heating of the background ions. However, the beam ions have been heated about a factor of eight, and there are oscillations in v_y reminiscent of those seen with growing waves (Figure 5.4). While there are no growing waves in this simulation, there are in the plasma stable magnetosonic modes that are in resonance with the beam ions, causing these (test) ions to be heated. (If the beam density were not zero, there would be a feedback in the response of these ions back on the waves, leading to wave growth and hence an instability.) Generally, one finds a steady level of fluctuations and essentially linear heating of the beam. Both the fluctuation level and the heating decrease with the number of (background) ions per cell, as shown in Table 5.1. The heating rate is defined as $\alpha = [T_\perp(t) - T_\perp(0)]/T_\perp(0)\Omega_i t$, evaluated here at $\Omega_i t = 50$. As in the earlier test cases, we consider runs with 10, 20, 40, and 80 background ions/cell as well as the 40 ion/cell case with smoothing. The level of fluctuations decreases linearly with particle number. Including the smoothing decreases the fluctuation level another 30%. At smaller particle/cell number the heating rate decreases with the fluctuation level, but at higher particle numbers the heating is more constant. (As a result, we chose 80 particles/cell for the run
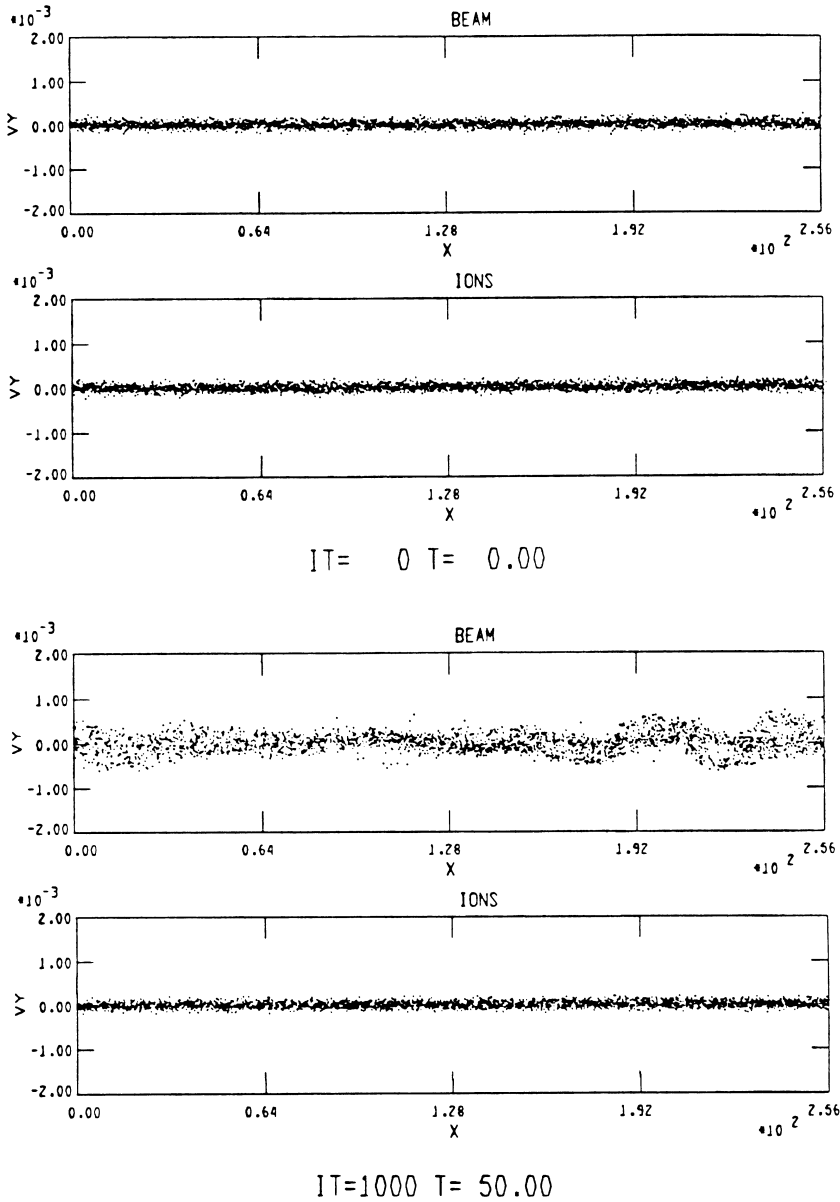
Figure 5.14: v_y-x phase space for the beam and background ions at $\Omega_i t = 0$ and $\Omega_i t = 50$, when $n_b = 0$, showing the amount of beam heating due to the background noise.

Table 5.1: Background fluctuation level and associated beam heating with number of background ions/cell ($n_b = 0$).

# background ions/cell	$(\delta B^2/B_o^2)$	heating rate: α
+10	0.026	0.73
+20	0.013	0.36
+40	0.0068	0.14
+80	0.0034	0.11
+40 (smoothed)	0.0045	0.16

in the previous subsection.) Smoothing does not have much effect on the beam heating (in fact, in this case the heating is slightly increased). Because the linear stability properties of the resonant electromagnetic ion/ion instability are not very sensitive to $T_\perp/T_\parallel$, it is not suprising that the overall characteristics of the instability (Figure 5.11) are not changed much, in spite of the beam heating due to noise. However, for other problems, particularly weak instabilities when one is trying to measure the amount of heating, it is something to keep in mind.

One can also investigate changes in the fluctuation level and the mode spectrum with system size, cell size, and time step, keeping in mind the restrictions on Δx and Δt discussed earlier. We leave this as an exercise for the reader. Hopefully, we also leave the reader with the impression that numerical tests are an important part of any simulation study and should be used often to verify the validity of the calculations.

5.3.3   Nonresonant electromagnetic ion/ion instability

At higher beam densities a second ion beam instability is excited, termed the nonresonant electromagnetic ion/ion instability. This instability is a fluid mode, driven by the anisotropy of the ion kinetic pressure, in analogy to the usual firehose mode in a single ion component plasma. At times in the foreshock, the beam density and/or velocity can be large enough to excite this mode [Sentman *et al.*, 1981]. Figure 5.15 shows the growth rate and real frequency for the resonant ($\omega_r > 0$) and nonresonant ($\omega_r < 0$) mode for $V_b/v_A = 10$, $n_b/n_o = 0.1$ and $\beta_e = \beta_i = \beta_b = 1$. For these parameters the maximum growth rates of the two modes are comparable, $\gamma_{max} \simeq 0.4\Omega_i$, but they occur at different wavenumbers: $kc/\omega_i \simeq 0.15$ (resonant), $kc/\omega_i \simeq 0.5$ (nonresonant). Thus, the nonresonant mode tends to grow at shorter wavelengths than the resonant mode. The real frequency for this mode is negative, *i.e.*, the waves propagate in the direction of the background ions (in the electron frame). To simulate this instability, we again take $NX = 128$, the same number of simulation particles
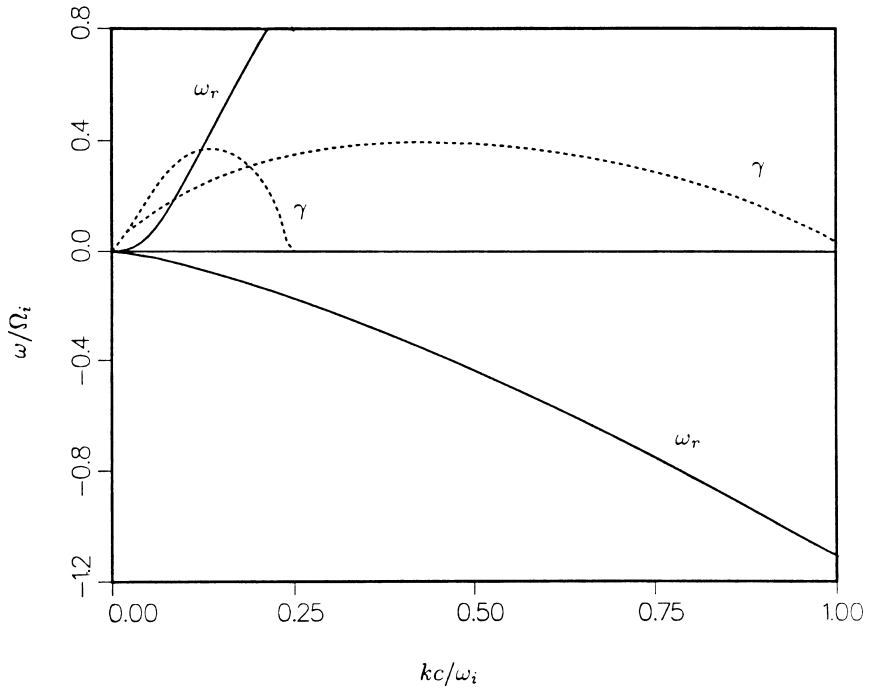
Figure 5.15: Results of linear theory for a larger beam density, $n_b/n_o = 0.1$ (other parameters same as Figure 5.3) showing growth rates (dashed curves) and ω_r (solid curves) for both the resonant mode ($\omega_r > 0$) and the nonresonant mode ($\omega_r < 0$).

(10240), but now reduce $XMAX$ to $128c/\omega_i$ ($HX = 1$) and also reduce $\Omega_i t = 0.025$.

Figure 5.16 shows results from the simulation at $\Omega_i t = 20$ (a little before the wave energy saturates). Displayed in a similar format to Figures 5.4- 5.6 are $x - v_x$ and $x - v_y$ phase space for the beam ions, the beam and background densities, B_y, and ϕ. Compared to the earlier case, here the beam is more violently scattered at comparable times to the resonant case, the wave amplitudes are much larger ($B_y/B_o \sim 2$), and there are large density fluctuations in both ion components. In this case v_y and B_y are in phase, and a predominant right hand sense of rotation of the wave is apparent from ϕ (negative helicity). The space-time profiles of B_y for both helicities are shown in Figure 5.17. At early times the dominant waves have negative helicity and initially propagate to the left with the background ions; these are the right hand polarized nonresonant modes. As the instability saturates, however, some of the wave fronts appear to stop and reverse direction. There are also positive helicity waves that are right hand polarized, which appear later. These are the resonant modes (cf. Figure 5.9). Figure 5.18 displays the time histories of δB^2 (total, top panel), δB^2 (negative helicity, middle panel), and δB^2 (positive helicity, lower panel). Consistent with the space-time plots of separate helicities, the shorter wavelength nonresonant modes grow up initially to large levels, but eventually the resonant, positive helicity waves grow to comparable amplitudes.

5.3.4 Electromagnetic ion cyclotron beam anisotropy instability

At smaller beam velocities ($V_b \sim v_A$) and higher beam densities ($n_b/n_o \sim 0.1$), an anisotropic beam ($T_{b\perp}/T_{b\parallel} > 1$) can be unstable to a left hand polarized Alfven ion cyclotron instability. Such an instability occurs in the equatorial magnetosphere and is responsible for the heating of minority ions [Gendrin *et al.*, 1984]. Figure 5.19 shows the characteristic growth rate and real frequency as a function of wavenumber for $n_b/n_o = 0.1$, $V_b = 0$, $\beta_{b\parallel} = 10$, $T_{b\perp}/T_{b\parallel} = 5$, $\beta_i = \beta_e = 1$ [Gary and Schriver, 1987]. In this case the instability is unstable over a wide range of wavenumbers with dominant wavelength $\lambda \simeq 20c/\omega_i$. With these beam parameters we thus take our simulation parameters to be: $NX = 128$, the total number of simulation particles $= 10240$, $XMAX = 128c/\omega_i$ and $\Omega_i \Delta t = 0.05$. Figure 5.20 shows the results of the simulation ($x - v_x$ and $x - v_y$ phase space for the beam ions, n_b, B_y, and ϕ profiles) at $\Omega_i t = 20$, about the time that wave growth ceases. The phase space and density show no remarkable features, other than the beam ions have been scattered into a nearly isotropic distribution, while the waves are generally smaller in amplitude ($\delta B/B_o \sim 0.4$). ϕ shows no well defined helicity, because there are waves of comparable amplitude propagating in both directions. Space time profiles of B_y separated by helicity (Figure 5.21) confirm this. The waves propagate in
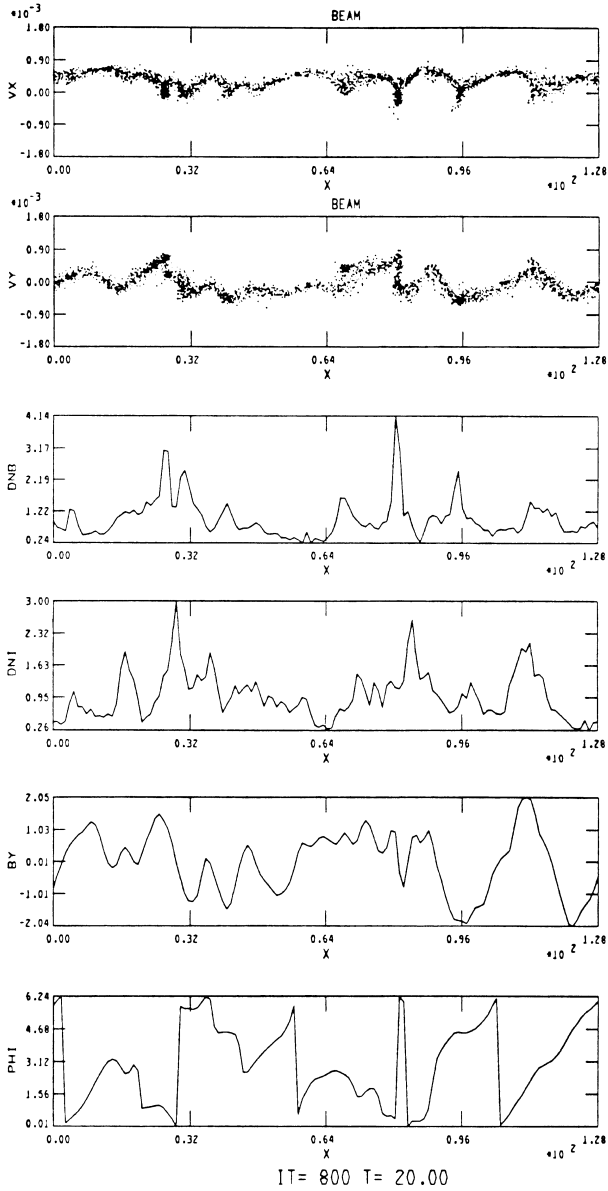
Figure 5.16: Results of simulations for the higher density case at $\Omega_i t = 20$: $x - v_x$ and $x - v_y$ phase space for beam ions, profiles of beam and background densities, B_y, and ϕ.
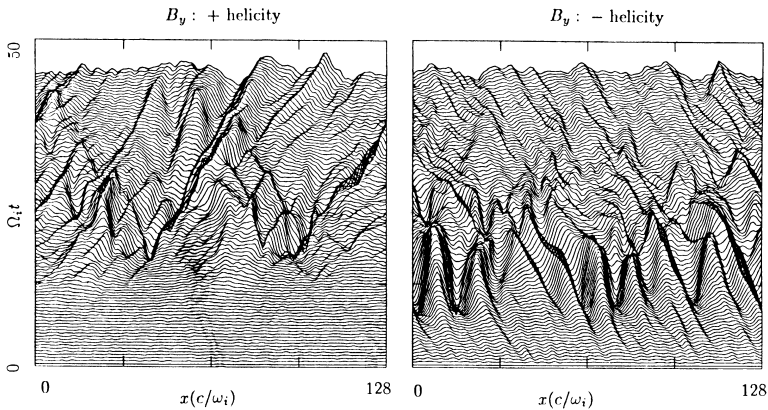
Figure 5.17: Space-time profiles of B_y for this case, in the same format as Figure 5.10.

opposite directions (negative helicity modes to the right and positive helicity modes to the left), and they are evidently left hand polarized. We leave it to the reader to go on to include a third ion species to study the heating of minority ions [*e.g.*, Omura *et al.*, 1985].

Also left as an exercise is to examine instabilities when $\vec{k}$ is not aligned along $\vec{B}_o$. One can simulate, for example, the resonant electromagnetic ion/ion instability at oblique propagation to study wave steepening effects [*e.g.*, Omidi and Winske, 1990] or other electromagnetic ion beam instabilities, *e.g.*, the electromagnetic ion/ion cyclotron instability [Winske and Omidi, 1990].

5.3.5 Modifying the Code

To treat more complex problems we must go into the code and modify it appropriately. We briefly discuss three types of changes that are most useful and cite examples where they have been employed.

The first type of change involves the initial conditions of the ion species, for example, including a finite length beam or a different velocity distribution (*e.g.*, a ring-beam). In this case we merely need to change the particle loading in subroutine INIT. For a finite length beam one also needs to modify the variable DFAC, which relates the number of simulation particles to normalized density. Examples of changes of this type include the study of instabilities with a ring-beam distribution [Winske *et al.*, 1985b] and the interaction of a finite length beam with a background plasma [Onsager *et al.*, 1991].

A second type of change involves the injection of ions, for example, to study
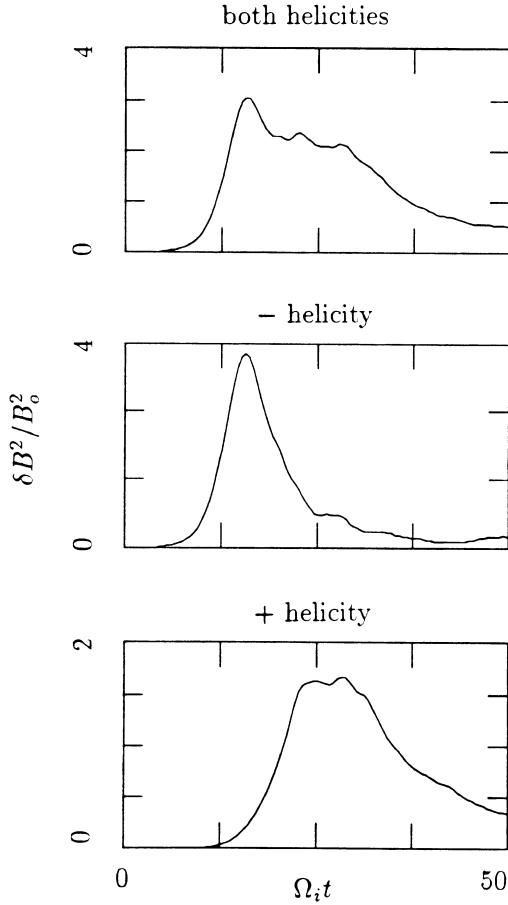
Figure 5.18: Time histories of magnetic field fluctuations: [top] $\delta B^2/B_o^2$; [middle] $\delta B^2/B_o^2$ (negative helicity component only); [bottom] $\delta B^2/B_o^2$ (positive helicity component only).
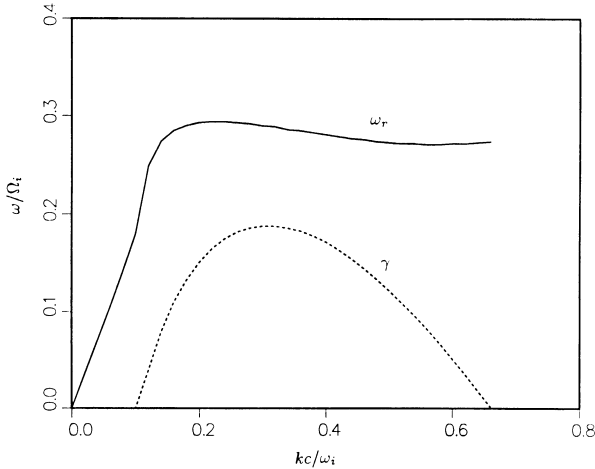
Figure 5.19: Results of linear theory for the electromagnetic ion cyclotron beam anisotropy instability ($n_b/n_o = 0.1$, $V_b/v_A = 0$, $T_{b\perp}/T_{b\|} = 5$, $\beta_{b\|} = 10$, $\beta_i = \beta_e = 1$): γ (dashed curve) and ω_r (solid curve).

active experiments and comets [Gary *et al.*, 1988; Miller *et al.*, 1991]. In this case the modifications are more extensive. First, the density normalization is different: n_o is taken to be the density of the fixed background ion population rather than that of the total density. The time varying density of the injected beam ions depends on the number of ions injected per time step as well as a normalizing parameter that takes the place of the variable FRAC. Second, we must leave room in storage for the ions that will be injected throughout the run; this is done when specifying $NSPEC$ for each species. Third, we must decide on how many ions to inject at each time step in TRANS, and then in PARMOV give these newborn ions velocities and positions and move them accordingly. An alternative way to proceed would be to initialize all the ions at $t = 0$, but only start to move them at the appropriate time.

A third type of modification involves changing the boundary conditions. For example, a common type of problem studied by hybrid codes involves the generation of collisionless shocks. Shocks can be produced by several different methods, but the "hard wall" method has become the most commonly used. In this method the incident ions, which have directed velocity $V_o\hat{x}$, are reflected off the right boundary at $x = XMAX$. The incident and reflected streams then interact to produce a heated downstream state and a shock that propagates out ahead to the left. Typically, V_o is chosen to be $V_o = V_1 - V_2$, where $V_1 = M_A v_A$
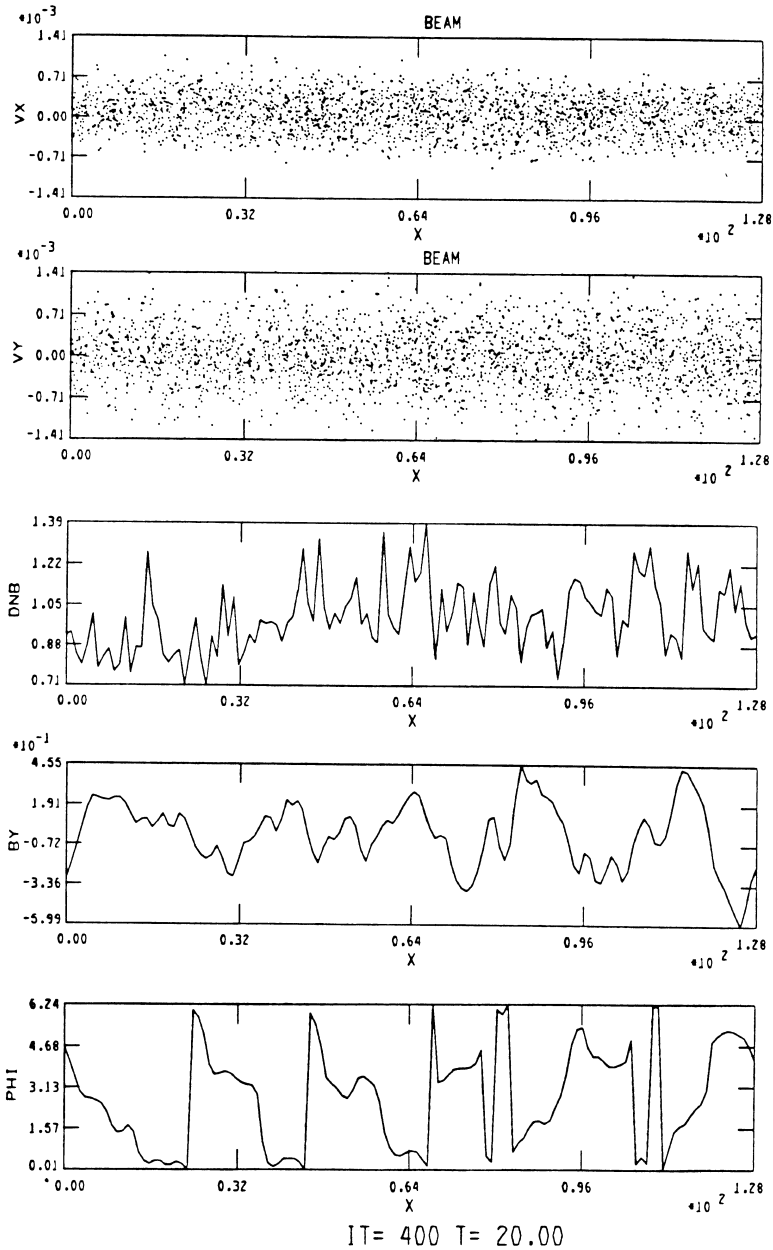
Figure 5.20: Results of hybrid simulations for this case: $x - v_x$ and $x - v_y$ phase space for the beam ions, and profiles of the beam density, B_y, and ϕ at $\Omega_i t = 20$.
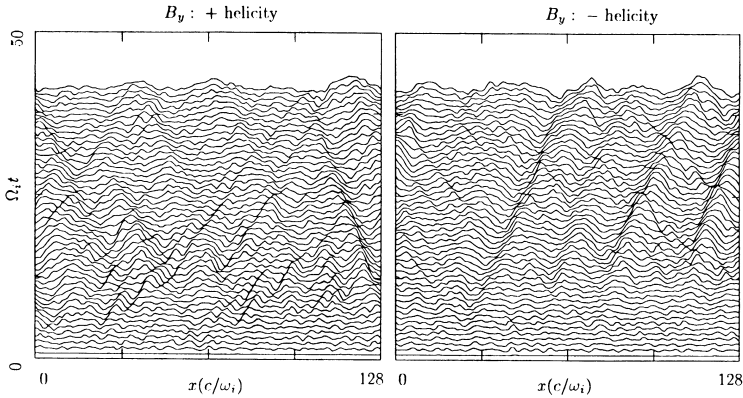
Figure 5.21: Space-time profiles of B_y for this case in the same format as Figure 5.10.

is the desired Alfven Mach number of the shock and V_2 is the downstream flow velocity calculated from the Rankine-Hugoniot relations. In this case the simulation frame corresponds to the downstream (plasma) frame of the shock.

To modify the code accordingly, numerous changes are again necessary. First, injection of new ions (see above) is needed to maintain the flow of the incident stream into the simulation domain at $x = 0$. Second, the particle boundary conditions are altered so that the ions are specularly reflected at the end of the box. For example, if a particle's new position, x_p^{N+1}, is greater than $XMAX$, we set

$$x_p^{N+1} = XMAX - (x_p^{N+1} - XMAX) \qquad (5.91)$$

and

$$v_{p,x}^{N+1} = -v_{p,x}^{N+1} \qquad (5.92)$$

Similar conditions are imposed for particles with $x_p^{N+1} < 0$; the particles can either be reflected, reinjected with the incident stream, or removed from the system. Third, the ion densities and currents collected in the ghost cells are put into adjacent cells, rather than at opposite ends: *e.g.*, the contributions to n_i collected at $I = 1$ goes to the cell $I = 2$ and the contribution collected at $I = NX2$ is placed in cell $I = NX1$. Fourth, the field solver is modified (in fact, simplified), as discussed in Section IID. In this case suitable boundary conditions are: $E_y = (V_1 - V_2)B_{zc}$, $E_z = -(V_1 - V_2)B_{yc}$, $E_x = 0$ at $x = 0$ (B_{yc} and B_{zc} are the upstream uniform fields). At the right boundary we either fix B_y and B_z to their values specified by the Rankine-Hugoniot conditions and set the x-derivative of the electric field equal to zero, or set $E_y = E_z = E_x = 0$ and

the x-derivative of B_y and B_z equal to zero. Similarly, we take n_i, J_{iy}, and J_{iz} to be continuous and $J_{ix} = 0$ at each end.

Collisionless shocks have been studied extensively by means of 1-D hybrid codes. The two most significant parameters for characterizing shocks are the Alfven Mach number M_A and θ_{Bn}, the angle between the shock normal direction $\hat{n} = -\hat{x}$ and the upstream magnetic field. Shocks with $\theta_{Bn} > 45^o$ are termed quasi-perpendicular shocks. Quasi-perpendicular shocks with $M_A > 3$ ("supercritical shocks") have been studied by Leroy *et al.* [1981, 1982] and more recently by Burgess *et al.* [1989]. A good introduction is given by Goodrich [1985]. Quasi-parallel shocks ($\theta_{Bn} < 45^o$) have also been well studied [Kan and Swift, 1983; Mandt and Kan, 1985; Quest, 1988]. In recent years they have been the target of much work [Burgess, 1989; Lyu and Kan, 1990; Scholer and Terasawa, 1990; Thomas *et al.*, 1990; Winske *et al.*, 1990; Omidi *et al.*, 1990] because of their inherent unsteadiness and the tendency of the shock front to undergo a cyclic disintegration and then reformation.

Unsteady shock behavior can also occur in the quasi-perpendicular regime at very high Mach numbers [Quest, 1986] in the absence of sufficient resistivity. Collisionless shocks with $M_A < 1$ (slow shocks) have also been simulated [Swift, 1983; Winske *et al.*, 1985a; Omidi and Winske, 1989; Lee *et al.*, 1989] as well as intermediate shocks ($M_A \simeq 1$) [Wu and Hada, 1991b]. More complex studies of shocks have included the interaction of two quasi-perpendicular shocks [Cargill and Goodrich, 1987] and the bow shock generated in the exosphere of a comet [Omidi and Winske, 1987]. Hybrid codes have also been used to study the structure of discontinuities other than shocks, *e.g.*, tangential [Cargill, 1990] and rotational [Lee *et al.*, 1989; Richter and Scholer, 1990; Goodrich and Cargill, 1991; Wu and Hada, 1991a] discontinuities. In these later cases one again uses plasma injection at one end of the simulation, but initializes the calculation with the discontinuity already in place separating two uniform (upstream, downstream) states, as was done in early shock studies [Leroy *et al.*, 1981, 1982].

5.4   Discussion

Thus far, we have motivated the need for and the usefulness of a hybrid plasma description in which ion kinetics are retained and electrons are represented as a massless fluid. The details of a simple 1-D hybrid code have been discussed, and test problems and applications have been illustrated. At this stage the reader should be able to go on to set up, run, and understand the results of his or her particular problem. Before concluding this chapter, however, we wish to briefly address the extension of hybrid codes to higher spatial dimensions, mention some of the state of the art calculations that are being carried out at present, and indicate some future trends.

It should be emphasized that we have discussed here only one method of

solving the electromagnetic fields in a 1-D hybrid code. Other methods have been devised and work as well as, if not better than, the one described here. Recall that the basic problem is to advance $\vec{E}^N$, $\vec{B}^N$ to the next time level when x_p^N and $\vec{v}_p^{N+1/2}$ are known. The method we use extrapolates $\vec{v}_p^{N+1/2} \rightarrow v_p^{N+1}$ to get the currents and density at time level $N + 1$. Other methods employ a predictor-corrector scheme [Harned, 1982], a Runge-Kutta scheme [Terasawa *et al.*, 1986] involving a subdivided time step to solve an implicit equation for $\vec{B}^{N+1}$, and an implicit method involving the solution of an ion moment equation [Quest, 1989] or a direct extrapolation of the ion current [Thomas *et al.*, 1990]. Some of these methods are discussed and compared in Winske [1985] and Quest [1989]. In one dimension they work about equally well and the tradeoff between accuracy and efficiency is not much of a problem.

In higher dimensions, however, the tradeoff becomes more significant, and some of the schemes are more readily adaptable. The predictor-corrector scheme is easily generalized and has been applied to numerous problems [Thomas and Brecht, 1986; Brecht and Thomas, 1987, 1988; Winske and Quest, 1986, 1988], although it is somewhat slower because it requires two passes through the particles each time step. Likewise, the Terasawa scheme [1986] requires an iteration involving the particles. Quest's [1989] scheme suffers from the lack of an easy generalization to multiple species with different charge to mass ratios. The resistive scheme discussed here requires a more complex decomposition and field solver [Hewett, 1980]. An iterative field solver that works in 3-D has also been developed [Horowitz *et al.*, 1989]. None of these schemes, however, have been tested against each other in a quantitative manner on a 2-D test problem. However, as 2-D hybrid codes come into wider use, such comparisons will certainly be conducted.

Two and three dimensional calculations, however, have been carried out and illustrate the degree of complexity and new understanding that such simulations can give. The major bottleneck of large scale simulations seems to be the limited analysis and visualization tools that are available rather than the algorithms themselves. We briefly discuss three examples.

Thomas and Winske [1990] have studied the formation of and ion dynamics at a curved bow shock. Figure 5.22 shows the formation of the shock, in which are plotted shaded density contours at three times. The arrow indicates the direction of the upstream magnetic field; the plasma flows in from the right. A key ingredient of the simulation is to allow the ions to interact with the "magnetosphere", which in this case is a solid object, only the edge of which lies at the left end of the simulation domain, in such a way that a steady state shock can form. In these calculations the particles bounce off the object, drift upwards out of the simulation plane, and escape over it out of the system, thus allowing a steady shock to eventually be set up. At late times some ions have escaped upstream of the shock to begin forming the foreshock. The 2-D simulations demonstrate that the energetic ions found in the foreshock result
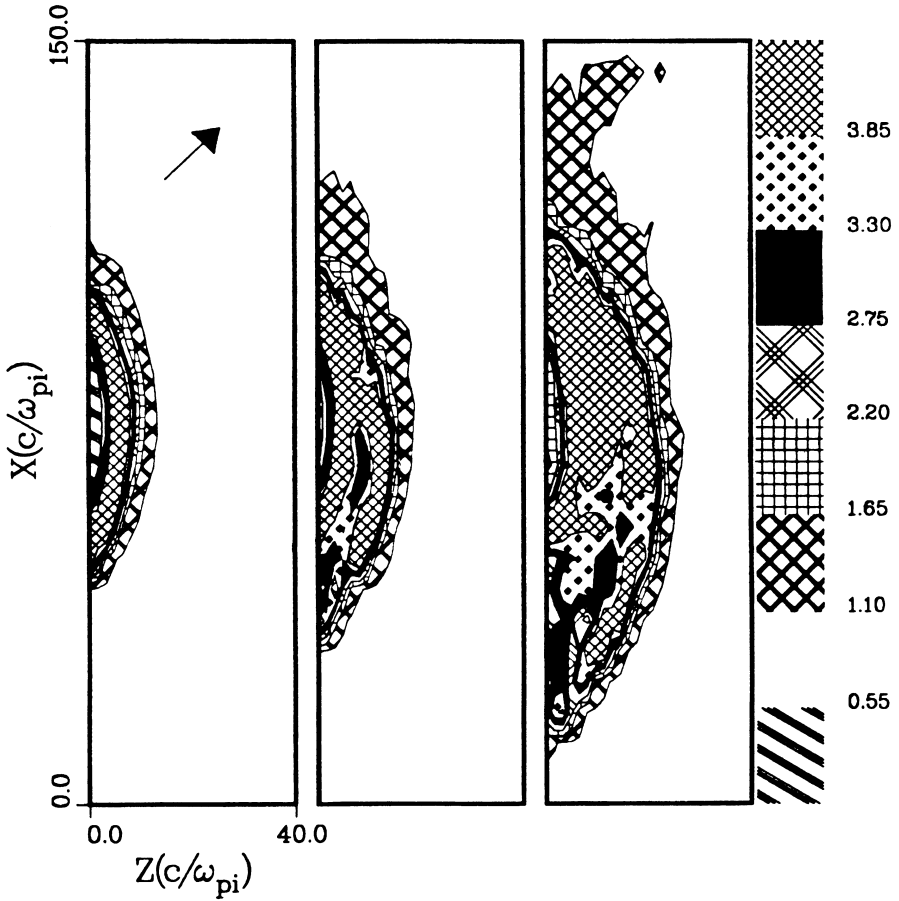
Figure 5.22: Formation of a curved bow shock from a 2-D hybrid simulation by Thomas and Winske [1990], showing shaded density contours at three times in the run.
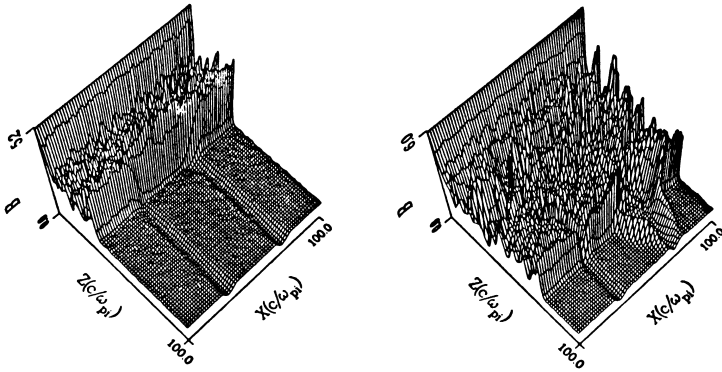
Figure 5.23: Results of 2-D hybrid simulations of the interaction of two current sheets in the upstream region with a quasi-perpendicular shock showing B at two times: [left panel] beginning of the interaction; [right panel] formation of a hot diamagnetic cavity at the shock [Thomas *et al.*, 1991].

primarily from shock drift acceleration, *i.e.*, gaining energy from the shock electric field as they drift along the surface of the shock. Other large scale 3-D simulations have been carried out for the bow shock of Venus [Brecht, 1990; Moore *et al.*, 1991] that show the structure of the shock and corresponding ion dynamics (of both solar wind and planetary origin). In this case the flow of the ions around the object is naturally included, but at the expense of much poorer resolution.

The interaction of a current sheet in the upstream flow with a planar shock has also been recently done in 2-D [Thomas *et al.*, 1991]. The interaction of ions reflected at the shock with the current sheet produces a low density cavity filled with these energized ions that exclude the incoming plasma and magnetic field. Figure 5.23 shows a 3-D perspective of the magnetic field magnitude at two times. The left panel shows two current sheets in the upstream flow encountering the shock (which is propagating to the right in the figure). The right panel shows a similar perspective somewhat later in time. At the lower current sheet little happens. At the upper current sheet, however, one sees that a magnetic cavity has formed at the shock that extends both downstream as well as into the upstream region. Enhancements of the magnetic field (and density) form at the edges of the cavity. Such "hot diamagnetic cavities" or "hot flow anomalies" have been observed in the vicinity of the bow shock [*e.g.*, Thomsen *et al.*, 1986]. The observations, however, have not been able to establish the origin of such structures and determine whether they are attached to the shock or freely propagating in the upstream solar wind. The simulations provide a

clear explanation, verify and extend previous test particle calculations of this process [Burgess, 1989], which first predicted that one of the current sheets will make a cavity and the other will not, and suggest further observational tests.

Finally, 3-D hybrid simulations of active experiments, such as AMPTE, have been carried out [Brecht and Thomas, 1987; 1988; Bingham *et al.*, 1991]. The simulations show how the released ions move with respect to the ambient plasma and expand to form a cavity. The surface of the expanding plasma is also subject to an instability, which leads to the formation of field aligned striations. Figure 5.24, from Brecht and Thomas [1988], shows some results of a 3-D calculation of an AMPTE release. The initial configuration, two perspectives of the magnetic field (one showing the formation of a diamagnetic cavity), and the background ion density are displayed. Again, the simulations have been instrumental in sorting out the forces on the released ions and their interaction with the background plasma. Such types of calculations should prove to be extremely useful in interpreting the recent CRRES releases.

In the years ahead, we expect that hybrid codes will continue to be major contributors to the understanding of space plasma phenomena. As more powerful computers become more readily available, we expect to see larger and more complex 2-D and 3-D calculations. We will also see the inclusion of more physics, *e.g.*, more ion species, complex charge states and rudimentary chemistry to couple them together, collisional processes to model ionospheric effects, *etc.* We anticipate the rapid growth and increased sophistication of high speed graphics and visualization techniques, which are absolutely essential for 3-D calculations. With the development of parallel architecture machines, even larger scale problems involving sizable segments of the entire magnetosphere are no longer out of the question. We remain convinced, however, of the continued need for a detailed understanding of the underlying physics, the development of modules for localized processes, and the testing of simple models: much of this will remain in the domain of 1-D calculations.
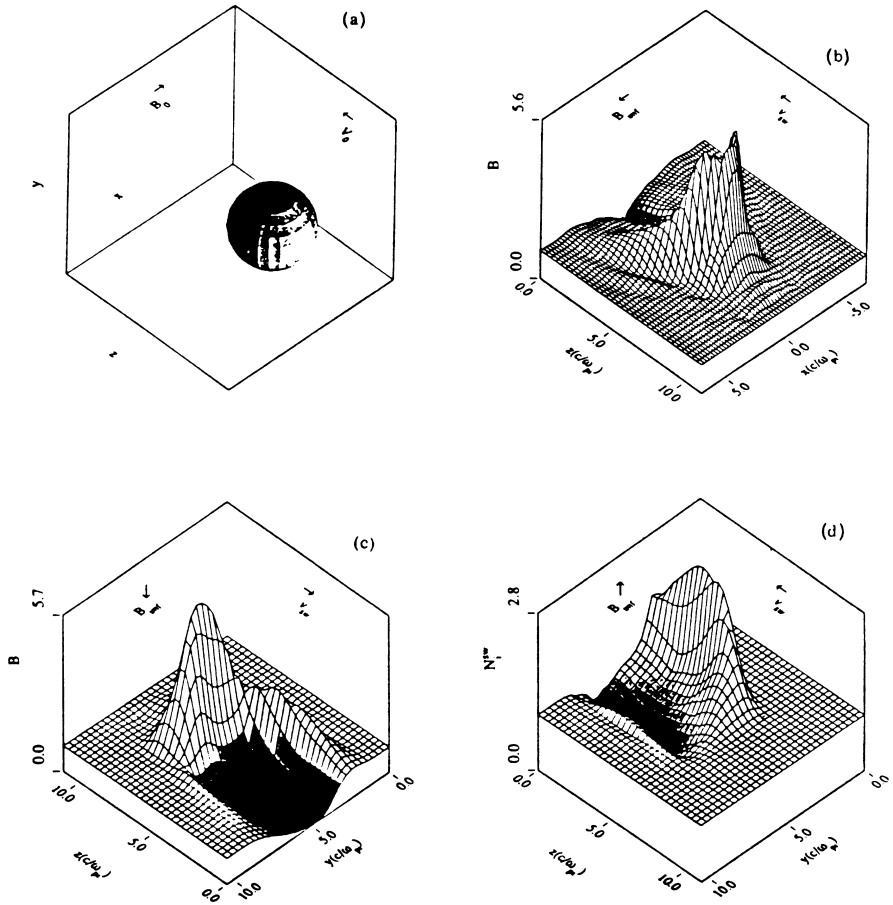
Figure 5.24: Results of a 3-D simulation of an AMPTE release [Brecht and Thomas, 1988] showing the initial configuration, two perspectives of the magnetic field, and the background ion density.

Appendix A: Ion Dynamics

In this appendix the ion equation of motion and how it is solved is discussed in some detail. Starting with $d\vec{X}/dt = \vec{V}$, we let $\vec{X}^N$ be the position of an ion at time $t = N\Delta t$. Then the left hand side of this equation in finite difference form becomes:

$$L.H.S. = \frac{\vec{X}^{N+1} - \vec{X}^N}{\Delta t} \tag{5.93}$$

To make the differencing time centered, we need to know $\vec{V}^{N+\frac{1}{2}}$. Thus,

$$\vec{X}^{N+1} = \vec{X}^N + \Delta t\, \vec{V}^{N+\frac{1}{2}} \tag{5.94}$$

The ion equation of motion is:

$$m_s \frac{d\vec{V}^{N+\frac{1}{2}}}{dt} = e_s \left(\vec{E} + \vec{V} \times \vec{B} \right) - e_s \eta \vec{J} \tag{5.95}$$

For the above equation to be time centered, we need $\vec{E}^N$, $\vec{V}^N$, $\vec{B}^N$, and $\vec{J}^N$. This then implies that the electromagnetic fields used to push the particle are those at time step N. Note, however, that velocity and current are also needed at time step N. The way in which we obtain $\vec{J}^N$ will be discussed later. For $\vec{V}^N$ we use $\vec{V}^N = \frac{1}{2}(\vec{V}^{N-\frac{1}{2}} + \vec{V}^{N+\frac{1}{2}})$. The above equation can then be written as:

$$\vec{V}^{N+\frac{1}{2}} = \vec{V}^{N-\frac{1}{2}} + \frac{e_s \Delta t}{m_s} \left(\vec{E}^N - \eta \vec{J}^N + \frac{1}{2}(\vec{V}^{N+\frac{1}{2}} + \vec{V}^{N-\frac{1}{2}}) \times \vec{B}^N \right) \tag{5.96}$$

To rewrite this equation in a simpler form we define the following:

$$h \equiv \frac{e_s \Delta t}{m_s}, \vec{E}' \equiv \vec{E}^N - \eta \vec{J}^N, m \equiv N + \frac{1}{2}, n \equiv N - \frac{1}{2} \tag{5.97}$$

Then,

$$\vec{V}^m = \vec{V}^n + h \left(\vec{E}' + \frac{1}{2}(\vec{V}^m + \vec{V}^n) \times \vec{B}^N \right) \tag{5.98}$$

To solve for $\vec{V}^m$, we first find the dot product of (5.98) and $\vec{B}^N$:

$$\vec{B}^N \cdot \vec{V}^m = \vec{B}^N \cdot \vec{V}^n + h\, \vec{B}^N \cdot \vec{E}' + \frac{h}{2} \vec{B}^N \cdot (\vec{V}^m + \vec{V}^n) \times \vec{B}^N$$

$$\Rightarrow \vec{B}^N \cdot \vec{V}^m = \vec{B}^N \cdot \vec{V}^n + h\vec{B}^N \cdot \vec{E}' \tag{5.99}$$

Next we find the cross product of (5.98) and $\vec{B}^N$, which involves a number of terms; writing only that involving $\vec{V}^m$ we get:

$$\vec{V}^m \times \vec{B}^N = \cdots + \frac{1}{2}(\vec{V}^m \times \vec{B}^N) \times \vec{B}^N + \cdots$$

$$= \cdots + \frac{1}{2}(\vec{B}^N \cdot \vec{V}^m)\vec{B}^N - \frac{1}{2}(\vec{B}^N \cdot \vec{B}^N)\vec{V}^m + \cdots \tag{5.100}$$

Substituting Equation (5.99) into (5.100) and Equation (5.100) back into (5.98), after some rearranging we get:

$$\left(1 + \frac{h^2}{4}(\vec{B}^N \cdot \vec{B}^N)\right)\vec{V}^m = \vec{V}^n(1 - \frac{h^2}{4}\vec{B}^N \cdot \vec{B}^N)$$

$$+h(\vec{E}' + \vec{V}^n \times \vec{B}^N) + \frac{h^2}{2}(\vec{E}' \times \vec{B}^N)$$

$$+\frac{h^2}{2}(\vec{B}^N \cdot \vec{V}^n)\vec{B}^N + \frac{h^3}{4}(\vec{B}^N \cdot \vec{E}')\vec{B}^N$$

$$(5.101)$$

which is the same as Equation (5.12) in the text. Dropping terms of the order Δt^3 and higher, Equation (5.101) reduces to:

$$\vec{V}^m = \vec{V}^n(1 - \frac{h^2}{2}\,\vec{B}^N \cdot \vec{B}^N) + h(\vec{E}' + \vec{V}^n \times \vec{B}^N)$$

$$+\frac{h^2}{2}\left((\vec{B}^N \cdot \vec{V}^n)\,\vec{B}^N + \vec{E}' \times \vec{B}^N\right) \qquad (5.102)$$

which is the same as Equation (5.13). By defining the following parameters:

$$f \equiv 1 - \frac{h^2}{2}\,(\vec{B}^N \cdot \vec{B}^N)\,,\ g \equiv \frac{h}{2}(\vec{B}^N \cdot \vec{V}^n)$$

$$\vec{V}^o \equiv \vec{V}^n + \frac{h}{2}\,\vec{E}' \qquad (5.103)$$

Equation (5.102) is rewritten as:

$$\vec{V}^m = f\,\vec{V}^n + h\,(\vec{E}' + g\,\vec{B}^N + \vec{V}^o \times \vec{B}^N) \qquad (5.104)$$

This is the form in which ion equation of motion is cast in the hybrid code. Given $\vec{V}^{N+\frac{1}{2}}$, we would also like to calculate $\vec{V}_i^{N+1}$ (average ion velocity at $t = (N + 1)\Delta t$). $\vec{V}_i^{N+1}$ is needed in order to calculate $\vec{J}^{N+1}$, which in turn is needed to obtain $\vec{E}^{N+1}$, $\vec{B}^{N+1}$ and also during the next particle push. To obtain $\vec{V}_i^{N+1}$ we push the ions half a time step using:

$$\vec{V}^{N+1} = \vec{V}^{N+\frac{1}{2}} + \frac{h}{2}\left(\vec{E}'^N(X^{N+1}) + \vec{V}^{N+\frac{1}{2}} \times \vec{B}^N(X^{N+1})\right) \qquad (5.105)$$

where the fields from time step N at the ion's new position (X^{N+1}) are used.

Appendix B: Magnetic Helicity

Helicity decribes the sense of rotation in space of a wave with respect to $\vec{k}$. As it is determined at a fixed time, the helicity is a convenient quantity to

compute in the simulation. Because it is a function of wavenumber and not frequency, it is not subject to Doppler shift and hence is independent of the frame in which it is measured. However, a particular mode may not have a unique helicity [e.g., Gary, 1986], and hence, it can be a useful diagnostic, but one that cannot be used by itself to identify wave modes.

To decompose a wave into helical parts, we expand it in a Fourier series:

$$B_y = \sum_k B_y^c \cos kx - B_y^s \sin kx \tag{5.106}$$

$$B_z = \sum_k B_z^c \cos kx - B_z^s \sin kx \tag{5.107}$$

(Note that unlike Terasawa *et al.* [1986], the sin terms in (5.106-5.107) have a minus sign, which is consistent with the Fourier transform routine supplied with the hybrid code.)

We define helical components, B^+, B^-, as

$$B^+ = \frac{1}{2}[(B_y^c + B_z^s) + i(B_z^c - B_y^s)] \tag{5.108}$$

$$B^- = \frac{1}{2}[(B_y^c - B_z^s) + i(B_z^c + B_y^s)] \tag{5.109}$$

where $+$ and $-$ refer to spirals with left and right hand sense of rotation with respect to the positive x direction (here assumed to be the direction of the magnetic field and $\vec{k}$). These spiral modes can be written as

$$B^+(x,t) = \sum_k B^+(k,t)e^{-ikx} \tag{5.110}$$

$$B^-(x,t) = \sum_k B^-(k,t)e^{+ikx} \tag{5.111}$$

and hence

$$B_y^+ = Re[B^+(x,t)] \tag{5.112}$$

$$B_z^+ = Im[B^+(x,t)] \tag{5.113}$$

$$B_y^- = Re[B^-(x,t)] \tag{5.114}$$

$$B_z^- = Im[B^-(x,t)] \tag{5.115}$$

which can then be related to the original Fourier decomposition, using (5.108-5.109).

As discussed in the text, the positive helicity mode corresponds to a right hand polarized wave propagating in the $+x$ direction and a left hand polarized wave propagating in the $-x$ direction. Similarly, the negative helity mode corresponds to a left hand polarized wave propagating in the $+x$ direction and a right hand polarized wave propagating in the $-x$ direction. As noted above,

shifting reference frames (e.g., from the background ion to the beam frame) does not change the helicity. However, the direction that the waves propagate, and hence the polarization, may change.

For parallel propagating waves, the helicity has the value of ±1. In general, however, the helicity is calculated using [Gary, 1986]

$$\sigma(\vec{k}) \;=\; \frac{k < \vec{A}(\vec{k}) \cdot \vec{B}(\vec{k}) >}{|\vec{B}|^2} \tag{5.116}$$

where, as usual, $\vec{B} = \vec{\nabla} \times \vec{A}$.

References

Akimoto, K., and D. Winske, Generation of strong MHD Alfvenic turbulence, *Phys. Rev. Lett., 64*, 753, 1990.

Aldrich, C. H., Particle code simulations with injected particles, *Space Sci. Rev., 42*, 131, 1985.

Anderson, R. R., G. K. Parks, T. E. Eastman, D. A. Gurnett, and L. A. Frank, Plasma waves associated with energetic particles streaming into the solar wind from the Earth's bow shock, *J. Geophys. Res., 86*, 4493, 1981.

Barnes, A., Theory of generation of bow shock associated hydromagnetic waves in the upstream interplanetary medium, *Cosmic Electrodynamics, 1*, 90, 1970.

Bingham, R., R. Bollens, F. Kazeminejad, and J. M. Dawson, Simulation studies of an interaction of a neutral gas and an ambient plasma, in *Cometary Plasma Processes*, edited by A. Johnstone, AGU Monogr. Ser., Vol. 61, Washington DC, 1991.

Brecht, S. H., Magnetic asymmetries at unmagnetized planets, *Geophys. Res. Lett., 17*, 1243, 1990.

Brecht, S. H., and V. A. Thomas, Three dimensional simulation of an active magnetospheric release, *J. Geophys. Res., 92*, 2289, 1987.

Brecht, S. H., and V. A. Thomas, Multidimensional simulations using hybrid particle codes, in *Particle Methods in Fluid Dynamics and Plasma Physics*, edited by J. U. Brackbill and J. J. Monaghan, p. 135, North Holland, Amsterdam, 1988.

Burgess, D., Simulation of backstreaming ion beams formed at oblique shocks by direct reflection, *Ann. Geophysicae, 5*, 133, 1987.

Burgess, D., On the effect of a tangential discontinuity on ions specularly reflected at an oblique shock, *J. Geophys. Res., 94*, 472, 1989.

Burgess, D., Cyclic behavior at quasi-parallel collisionless shocks, *Geophys. Res. Lett., 16*, 345, 1989.

Burgess, D., W. P. Wilkinson, and S. J. Schwartz, Ion distributions and thermalization at perpendicular and quasi-perpendicular supercritical collisionless shocks, *J. Geophys. Res., 94*, 8783, 1989.

Cargill, P. J., Hybrid simulations of tangential discontinuities, *Geophys. Res. Lett., 17*, 1937, 1990.

Cargill, P. J., and C. C. Goodrich, The interaction of quasi-perpendicular shock waves in a collisionless plasma, *Phys. Fluids, 30*, 2504, 1987.

Forslund, D. W., Fundamentals of plasma simulation, *Space Sci. Rev., 42*, 3, 1985.

Gary, S. P., Low frequency waves in high beta collisionless plasma: polarization, compressibility, and helicity, *J. Plasma Phys., 35*, 431, 1986.

Gary, S. P., and D. Schriver, The electromagnetic ion cyclotron beam anisotropy instability, *Planet. Space Sci., 35*, 51, 1987.

Gary, S. P., J. T. Gosling, and D. W. Forslund, The electromagnetic ion beam instability upstream of the Earth's bow shock, *J. Geophys. Res., 86*, 6691, 1981.

Gary, S. P., C. D. Madland, N. Omidi, and D. Winske, Computer simulations of two pickup ion instabilities in a cometary environment, *J. Geophys. Res., 93*, 9584, 1988.

Gary, S. P., C. D. Madland, D. Schriver, and D. Winske, Computer simulations of electromagnetic cool ion beam instabilities, *J. Geophys. Res., 91*, 4188, 1986.

Gary, S. P., M. D. Montgomery, W. C. Feldman, and D. W. Forslund, Proton temperature anisotropy instabilities in the solar wind, *J. Geophys. Res., 81*, 1241, 1976.

Gendrin, R., M. Ashour-Abdalla, Y. Omura, and K. Quest, Linear analysis of ion cyclotron interactions in a multi-component plasma *J. Geophys. Res., 89*, 9119, 1984.

Goodrich, C. C., Numerical simulations of quasi-perpendicular collisionless shocks, in *Collisionless Shocks in the Heliosphere: Reviews of Current Research*, edited by B. T. Tsurutani and R. G. Stone, p. 153, AGU Monogr. Ser., Vol. 35, Washington DC, 1985.

Goodrich, C. C., and P. J. Cargill, Hybrid simulations of rotational discontinuities, *Geophys. Res. Lett., 18*, 65, 1991.

Harned, D. S., Quasi-neutral hybrid simulation of macroscopic plasma phenomena, *J. Comput. Phys., 47*, 452, 1982.

Hewett, D. W., A global method for solving the electron-field equations in a zero inertia electron hybrid plasma simulation code, *J. Comput. Phys., 38*, 378, 1980.

Hoppe, M. M., C. T. Russell, L. A. Frank, T. E. Eastman, and E. W. Greenstadt, Upstream hydromagnetic waves and their association with backstreaming ion populations: ISEE 1 and 2 observations, *J. Geophys. Res., 86*, 4471, 1981.

Horowitz, E. J., D. E. Shumaker, and D. V. Anderson, QN3D: A three-dimensional quasi-neutral hybrid particle-in-cell code with applications to the tilt mode instability in field reversed configurations, *J. Comput. Phys.,*

84, 279, 1989.

Hoshino, M. and T. Terasawa, Numerical study of the upstream wave excitation mechanism, 1. Nonlinear phase bunching of beam ions, *J. Geophys. Res., 90*, 57, 1985.

Kan J. R., and D. W. Swift, Structure of the quasi-parallel bow shock: Results of numerical simulations, *J. Geophys. Res., 88*, 6919, 1983.

Kovner, M. S., Instability of low frequency electromagnetic waves in a plasma traversed by a beam of charged particles, *Sov. Phys. JETP, 13*, 369, 1961.

Lee, L. C., L. Huang, and J. K. Chao, On the stability of rotational discontinuities and intermediate shocks, *J. Geophys. Res., 94*, 8813, 1989.

Lee, L. C., Y. Lin, Y. Shi, and B. T. Tsurutani, Slow shock characteristics as a function of distance from the X line in the magnetotail, *Geophys. Res. Lett., 16*, 903, 1989.

Leroy, M. M., C. C. Goodrich, D. Winske, C. S. Wu, and K. Papadopoulos, Simulation of a perpendicular bow shock, *Geophys. Res. Lett., 8*, 1269, 1981.

Leroy, M. M., D. Winske, C. C. Goodrich, C. S. Wu, and K. Papadopoulos, The structure of perpendicular bow shocks, *J. Geophys. Res., 87*, 5081, 1982.

Lyu, L. H., and J. R. Kan, Ion leakage, ion reflection, ion heating, and shock front reformation in a simulated supercritical quasi-parallel collisionless shock, *Geophys. Res. Lett., 17*, 1041, 1990.

Mandt, M. E., and J. R. Kan, Effects of electron pressure in quasi-parallel collisionless shocks, *J. Geophys. Res., 90*, 115, 1985.

Mauk, B. H., C. C. McIlwain, and R. L. McPherron, Helium cyclotron resonance within the Earth's magnetosphere, *Geophys. Res. Lett., 8*, 103, 1981.

Miller, R. H., T. I. Gombosi, S. P. Gary, and D. Winske, The direction dependence of magnetic fluctuations generated by cometary ion pickup, *J. Geophys. Res., 96*, 9479, 1991.

Moore, K. R., V. A. Thomas, and D. J. McComas, A global hybrid simulation of the solar wind interaction with the dayside of Venus, *J. Geophys. Res., 96*, 7779, 1991.

Morse, R. L., and C. W. Nielson, Numerical simulation of the Weibel instability in one and two dimensions, *Phys. Fluids, 14*, 830, 1971.

Omidi, N., and D. Winske, A kinetic study of solar wind mass loading and cometary bow shocks, *J. Geophys. Res., 92*, 13409, 1987.

Omidi, N., and D. Winske, Structure of slow magnetosonic shocks in low beta plasmas, *Geophys. Res. Lett., 16*, 907, 1989.

Omidi, N., and D. Winske, Steepening of kinetic magnetosonic waves into shocklets: Simulations and consequences for planetary shocks and comets, *J. Geophys. Res., 95*, 2281, 1990.

Omidi, N., K. B. Quest, and D. Winske, Low Mach number parallel and quasi-parallel shocks, *J. Geophys. Res., 95*, 20717, 1990.

Omura, Y., M. Ashour-Abdalla, R. Gendrin, and K. Quest, Heating of thermal helium in the equatorial magnetosphere: A simulation study, *J. Geophys.*

Res., 90, 8281, 1985.

Onsager, T. G., D. Winske, and M. F. Thomsen, Interaction of a finite length ion beam with a background plasma: Reflected ions at the quasi-parallel bow shock, J. Geophys. Res., 96, 1775, 1991.

Paschmann, G., N. Sckopke, I. Papamastorakis, J. R. Asbridge, S. J. Bame, and J. T. Gosling, Characteristics of reflected and diffuse ions upstream from the Earth's bow shock, J. Geophys. Res., 86, 4355, 1981.

Quest, K. B., Simulations of high Mach number collisionless perpendicular shocks in astrophysical plasmas, Phys. Rev. Lett., 54, 1872, 1986.

Quest, K. B., Theory and simulation of collisionless parallel shocks, J. Geophys. Res., 93, 9649, 1988.

Quest, K. B., Hybrid simulation, in Tutorial Courses: Third International School for Space Simulation, edited by B. Lembege and J. W. Eastwood, p. 177, Cepadues Ed., Toulouse, France, 1989.

Richter, P., and M. Scholer, On the stability of rotational discontinuities, Geophys. Res. Lett., 17, 1257, 1989.

Scharer, J. E., and A. W. Trivelpiece, Cyclotron wave instabilities in a plasma, Phys. Fluids, 10, 591, 1967.

Scholer, M., and T. Terasawa, Ion reflection and dissipation at quasi-parallel collisionless shocks, Geophys. Res. Lett., 17, 119, 1990.

Scudder, J. D., A. Mangeney, C. Lacombe, C. C. Harvey, T. L. Aggson, R. R. Anderson, J. T. Gosling, G. Paschmann, and C. T. Russell, The resolved current layer of a collisionless high beta supercritical quasi-perpendicular shock wave, 1. Rankine-Hugoniot geometry, currents, and stationarity, J. Geophys. Res., 91, 11019, 1986.

Sentman, D. D., J. P. Edmiston, and L. A. Frank, Instabilities of low frequency parallel propagating electromagnetic waves in the Earth's foreshock region, J. Geophys. Res., 86, 7487, 1981.

Sgro, A. G., and C. W. Nielson, Hybrid model studies of ion dynamics and magnetic field diffusion during pinch implosions, Phys. Fluids, 19, 126, 1976.

Spicer, D. S., R. W. Clark, and S. P. Maran, A model of the pre-Sedov expansion phase of supernova remnant-ambient plasma coupling and x-ray emission from SN 1987A, Ap. J., 356, 549, 1990.

Stone, R. G., and B. T. Tsurutani, Collisionless Shocks in the Heliosphere: A Tutorial Review, AGU Monogr. Ser., Vol. 34, Washington DC, 1985.

Swift, D. W., On the structure of the magnetic slow switch-off shock, J. Geophys. Res., 88, 5685, 1983.

Tanaka, M., Simulations of heavy ion heating by electromagnetic ion cyclotron waves driven by proton temperature anisotropy, J. Geophys. Res., 90, 6459, 1985.

Terasawa, T., Nonlinear dynamics of Alfven waves: Interactions between ions and shock upstream waves, Comp. Phys. Comm., 49, 193, 1988.

Terasawa, T., M. Hoshino, J. T. Sakai, and T. Hada, Decay instability of fi-

nite amplitude cicularly polarized Alfven waves: A numerical simulation of stimulated Brillouin scattering, *J. Geophys. Res., 91*, 4171, 1986.

Thomas, V. A., and S. H. Brecht, Two dimensional simulation of high Mach number plasma interactions, *Phys. Fluids, 29*, 2444, 1986.

Thomas, V. A., and D. Winske, Two dimensional hybrid simulation of a curved bow shock, *Geophys. Res. Lett., 17*, 1247, 1990.

Thomas, V. A., D. Winske, and N. Omidi, Reforming supercritical quasi-parallel shocks, 1. One and two dimensional simulations, *J. Geophys. Res., 95*, 18809, 1990.

Thomas, V. A., D. Winske, M. F. Thomsen, and T. G. Onsager, Hybrid simulations of a hot flow anomaly, *J. Geophys. Res., 96*, 11625, 1991.

Thomsen, M. F., J. T. Gosling, S. A. Fuselier, S. J. Bame, and C. T. Russell, Hot diamagnetic cavities upstream from the Earth's bow shock, *J. Geophys. Res., 91*, 2961, 1986.

Tsurutani, B. T., and R. G. Stone, *Collisionless Shocks in the Heliosphere: Reviews of Current Research*, AGU Monogr. Ser., Vol. 35, Washington DC, 1985.

Winske, D., Hybrid simulation codes with application to shocks and upstream waves, *Space Sci. Rev., 42*, 53, 1985.

Winske, D., and S. P. Gary, Electromagnetic instabilities driven by cool heavy ion beams, *J. Geophys. Res., 91*, 6825, 1986.

Winske, D. and M. M. Leroy, Diffuse ions produced by electromagnetic ion beam instabilities, *J. Geophys. Res., 89*, 2673, 1984a.

Winske, D., and M. M. Leroy, Hybrid simulation techniques applied to the Earth's bow shock, in *Computer Simulations of Space Plasmas*, edited by H. Matsumoto and T. Sato, p. 255, D. Reidel/Terra Sci., Hingham MA, 1984b.

Winske, D., and N. Omidi, Electromagnetic ion/ion cyclotron instability at slow shocks, *Geophys. Res. Lett., 17*, 2297, 1990.

Winske, D., and K. B. Quest, Electromagnetic ion beam instabilities: comparison of one and two dimensional simulations, *J. Geophys. Res., 91*, 8789, 1986.

Winske, D., and K. B. Quest, Magnetic field and density fluctuations at perpendicular supercritical collisionless shocks, *J. Geophys. Res., 93*, 9681, 1988.

Winske, D., N. Omidi, K. B. Quest, and V. A. Thomas, Reforming supercritical quasi-parallel shocks, 2. Mechanism for wave generation and front reformation, *J. Geophys. Res., 95*, 18821, 1990.

Winske, D., E. K. Stover, and S. P. Gary, The structure and evolution of slow mode shocks, *Geophys. Res. Lett., 12*, 295, 1985a.

Winske, D., C. S. Wu, Y. Y. Li, Z. Z. Mou, and S. Y. Guo, Coupling of newborn ions to the solar wind by electromagnetic instabilities and their interaction with the bow shock, *J. Geophys. Res., 90*, 2713, 1985b.

Wu, C. C., and T. Hada, On rotational discontinuities in both two-fluid and hybrid models, *J. Geophys. Res., 96*, 3755, 1991a.

Wu, C. C., and T. Hada, Formation of intermediate shocks in both two-fluid and hybrid models, *J. Geophys. Res., 96*, 3769, 1991b.

Zachary, A. L., B. I. Cohen, C. E. Max, and J. Arons, The long time evolution of a low density ion beam, *J. Geophys. Res., 94*, 2443, 1989.